



ESA Climate Change Initiative – Fire_cci

D2.1.3 - Algorithm Theoretical Basis Document (ATBD) for the AVHRR LTDR burned area product

Project Name	ECV Fire Disturbance: Fire_cci
Contract N°	4000126706/19/I-NB
Issue Date	19/11/2021
Version	1.0
Author	Gonzalo Otón, Emilio Chuvieco
Document Ref.	Fire_cci_D2.1.3_ATBD-AVHRR-LTDR_v1.0
Document type	Public

To be cited as: G. Otón, E. Chuvieco (2021) ESA CCI ECV Fire Disturbance: D2.1.3 Algorithm Theoretical Basis Document (ATBD) for the AVHRR-LTDR burned area product, version 1.0. Available at: <https://climate.esa.int/en/projects/fire/key-documents/>

	Fire_cci ATBD AVHRR-LTDR	Ref.:	Fire_cci_D2.1.3_ATBD-AVHRR-LTDR_v1.0			
		Issue	1.0	Date	19/11/2021	
		Page				2

Project Partners

Prime Contractor/ Scientific Lead & Project Management	UAH – University of Alcalá (Spain)
Earth Observation Team	UAH – University of Alcalá (Spain)
	UPM – Universidad Politécnica de Madrid (Spain)
	CNR-IREA - National Research Council of Italy – Institute for Electromagnetic Sensing of the Environment (Italy)
System Engineering	BC – Brockmann Consult (Germany)
Climate Modelling Group	MPIM – Max Planck Institute for Meteorology (Germany)
	CNRS - National Centre for Scientific (France)



Distribution

Affiliation	Name	Address	Copies
ESA	Clément Albergel (ESA)	clement.albergel@esa.int	electronic copy
Project Team	Emilio Chuvieco (UAH)	emilio.chuvieco@uah.es	electronic copy
	M. Lucrecia Pettinari (UAH)	mlucaresia.pettinari@uah.es	
	Joshua Lizundia (UAH)	joshua.lizundia@uah.es	
	Amin Khairoun (UAH)	amin.khairoun@uah.es	
	Gonzalo Otón (UAH)	gonzalo.oton@uah.es	
	Mihai Tanase (UAH)	mihai.tanase@uah.es	
	Consuelo Gonzalo (UPM)	consuelo.gonzalo@upm.es	
	Dionisio Rodríguez Esparragón (UPM)	dionisio.rodriguez@ulpgc.es	
	Ángel García Pedrero (UPM)	angelmario.garcia@upm.es	
	Daniela Stroppiana (CNR)	stroppiana.d@irea.cnr.it	
	Mirco Boschetti (CNR)	boschetti.m@irea.cnr.it	
	Thomas Storm (BC)	thomas.storm@brockmann-consult.de	
	Martin Böttcher (BC)	martin.boettcher@brockmann-cons...	
	Grit Kirches (BC)	grit.kirches@brockmann-consult.de	
Florent Mouillot (CNRS)	florent.mouillot@cefe.cnrs.fr		
Philippe Ciais (CNRS)	philippe.ciais@lscce.ipsl.fr		

	Fire_cci ATBD AVHRR-LTDR	Ref.:	Fire_cci_D2.1.3_ATBD-AVHRR-LTDR_v1.0			
		Issue	1.0	Date	19/11/2021	
		Page				3

Summary

This document presents the technical basis of the algorithms used to generate the AVHRR-LTDR Fire_cci Burned Area product v1.1. The document analyses the input requirements and the process to create the product, including the stages of the processor to get the burned area data and the formatting of the data to obtain the product publicly released.

	Affiliation/Function	Name	Date
Prepared	UAH	Gonzalo Otón Emilio Chuvieco	25/10/2021
Reviewed	UAH – Project Manager	M. Lucrecia Pettinari	25/10/2021
Authorized	UAH - Science Leader	Emilio Chuvieco	25/10/2021
Accepted	ESA - Technical Officer	Clément Albergel	19/11/2021

This document is not signed. It is provided as an electronic copy.

Document Status Sheet

Issue	Date	Details
O2.D1.v1.0	13/04/2018	First release of the document.
O2.D1.v1.1	13/06/2018	Addressing comments of ESA-CCI-FIRE-EOPS-MEM-18-0146
D2.1.3.v1.0	19/11/2021	Complete update of the document

Document Change Record

Issue	Date	Request	Location	Details
O2.D1v1.1	3/06/2018	UAH ESA	Page 3 Sections 3.1, 3.2, 5, 6 Figures 7, 8 and 9 Figures 10 and 11	Updated list of Project Team Minor changes in the text to clarify the information. Caption updated. Figures updated.
D2.1.3v1.0	19/11/2021	UAH	All document	Change of the deliverable number. All sections updated and document extended



Table of Contents

1	Introduction.....	8
1.1	Background.....	8
2	BA Algorithm description	8
2.1	General scheme.....	8
2.2	Input data	11
2.2.1	AVHRR-LTDR product	11
2.2.2	Land Cover	14
2.2.3	FireCCI51	14
2.3	Pre-processing of LTDR data	15
2.3.1	Composites	15
2.3.2	Cloud Masking	15
2.3.3	LTDR Burned Index (LBI).....	16
2.3.4	Burned area detection models.....	17
2.3.4.1	Random Forest parameter tests	19
2.3.4.2	Spatial nature of fire events.....	20
2.3.4.3	Global and boreal databases	21
2.4	Post-processing of model probabilities.....	21
2.4.1	Binary classifications and Solar zenith angle correction.....	21
2.4.1.1	DC sensitivity analysis	22
2.4.1.2	Otsu threshold	22
2.4.1.3	Solar Zenith Angle correction	24
2.4.2	Proportions	26
2.5	FireCCILT11 product	28
2.5.1	Accuracy assessment	29
	References.....	30
	Annex 1: Acronyms and abbreviations	38
	Annex 2: Inter-comparison.....	39
1	BA databases	39
1.1	Global BA products	39
1.2	Regional databases.....	39
1.2.1	Official perimeters and regional products	39
1.2.2	Regional BA studies	40
2	Results	40
2.1	Comparison with global BA products	40
2.2	Regional comparison with MODIS BA products	42
2.3	Comparison with reference fire perimeters and regional BA products	44
2.4	Comparison with regional BA studies	46
	Annex 3: Validation.....	47
1	Validation basis	47

	Fire_cci ATBD AVHRR-LTDR	Ref.: Fire_cci_D2.1.3_ATBD-AVHRR-LTDR_v1.0
		Issue 1.0 Date 19/11/2021
		Page 5

1.1	Landsat dataset.....	47
1.2	Pareto Boundary	47
2	Results	48

List of Tables

Table 1.	Changes in the BA algorithm from the FireCCILT10 Beta product.	9
Table 2.	Criteria to filter clouds in the AVH09 images. If one of the conditions is met, the pixel is filtered.	15
Table 3.	Correlation analysis between the Algerian desert pixel (23.80°N, 0.40°W) of the different variables of the synthetic index and LBI. The Pearson’s r is calculated for the time series of the study and for the AVHRR2 (1982-2000) and the AVHRR3 (2001-2018) period.	17
Table 4.	Annual and month correlation (r Pearson) between BA products. Month correlation between AVHRR2 era months and AVHRR3 era months.	41
Table 5.	Correlation analysis (r Pearson) between the number of observations, solar angle, and the BA of FireCCILT10 Beta and FireCCILT11 according to Global, tropical and extratropical regions, and the time series of each product. Time periods are grouped as the complete time series, the AVHRR2 period, and the AVHRR3 period.	42
Table 6.	Average BA in the continental regions for the MODIS (FireCCI51, MCD64A1) and AVHRR-LTDR (FireCCILT11) products in the common time series (2001-2018). Boreal North America (BONA), Temperate North America (TENA), Central America (CEAM), Northern Hemisphere South America (NHSA), Southern Hemisphere South America (SHSA), Europe (EURO), Middle East (MIDE), Northern Hemisphere Africa (NHAF), Southern Hemisphere Africa (SHAF), Boreal Asia (BOAS), Central Asia (CEAS), Southeast Asia (SEAS), Equatorial Asia (EQAS) and Australia and New Zealand (AUST).	43
Table 7.	Correlation analysis (r Pearson) between the SZA and FireCCILT11 according to Continental regions.	43
Table 8.	Correlation analysis (r Pearson) between FireCCILT11 in different regions, and the official perimeters and regional BA products. Time periods are grouped as the complete time series with official perimeters, the AVHRR2 period, and the AVHRR3 period.	45
Table 9.	Correlation analysis (r Pearson) between FireCCILT11 and the regional BA studies. Time periods are grouped as the complete time series with regional BA studies, the AVHRR2 period, and the AVHRR3 period.	46
Table 10.	Validation outcomes between the FireCCILT11 and the long-term degraded Landsat dataset. Purple represents the years when the Landsat period is lower or equal to one and a half months, and the long-unit is minimal (2-4 scenes Landsat); Blue is used when there are non-interpretable areas and the study area is reduced; Yellow, when there are Landsat 7 with SLC-Off, and Brown when the Landsat period is lower or equal to one and a half months and there are Landsat 7 with SLC-Off.	49

List of Figures

- Figure 1. FireCCILT11 algorithm is shown as a flowchart. Gray boxes are the input data where the algorithm starts. Orange/beige boxes are data to compare and validate the new BA product. Black lines mean that the process is running once per month or year, blue lines that the process is running twice per month or year, one per each RF model. Orange/beige lines are validation and inter-comparison. 10
- Figure 2: availability of LTDR v5.0 daily images for the full time series. 12
- Figure 3. Time series of solar zenith angle values for a stable pixel located in Sahara Desert -Mauritania (20.35°N, -8.3°W) - of the LTDR time series. The impact of sensor’s degradation produces a delay in the cross the pixel. 13
- Figure 4. Monthly composites used to create the RF models. Monthly models were created using LBI values from several months before and after the target period. For instance, the global RF model of August had as independent variables the LBI of August, LBI of five months before August (that is, March to July) and LBI of six successive months (September to February). The dependent variable was the target BA (FireCCI51) of each target month, in this example was the FireCCI51 of August. For the Boreal model winter months were discarded. 18
- Figure 5. Analysis to obtain the best number of samples is each tree according to Dice Coefficient in the time series 2001-2018. From 20k used in FireCCILT10 Beta version to 11M which is our computational limit. 10M was selected in FireCCILT11, due to its accurate/time relation..... 19
- Figure 6. Analysis to obtain the weight assigned to the burn class according to Dice Coefficient in the time series 2001-2018. From no weight to Balanced. 10% was used in FireCCILT11 and FireCCILT10 Beta version where it was set up in a similar parameter. 19
- Figure 7. Analysis to obtain the maximum depth of the trees according to Dice Coefficient in the time series 2001-2018. From 5 to None. None was used in FireCCILT10 Beta version and FireCCILT11. 20
- Figure 8. Analysis to obtain the years and the % of database to train the model according to Dice Coefficient. From 5% to 25% of samples to validate and 8 to 15 years to train the model. 10% and 8 years was used in FireCCILT10 Beta version and 25% and 18 years in FireCCILT11..... 20
- Figure 9. FireCCI51 BA average (2001-2018) per months according to high latitudes. 21
- Figure 10. Calculation of BA proportions per grid cells (0.25°). This example shows the four classification possibilities (A-D), where y is the year, m is the month, and CR is each of the continental regions. The figure shows in the upper left the sum of FireCCI51 BA of the different years (2001-2018) and in the lower left the sum of the Binary classification BA (obtained from the RF algorithm, and deemed fully burned). In the centre, the BA proportions allocated to each grid cell is shown, which multiplied by the BA in each Binary classification image in the 1982-2018 time series allows to obtain the total burned area in each pixel. 27
- Figure 11. Annual FireCCILT11 BA (at 0.25° resolution) for two different periods: (a) 1982 belongs to the 1982-2000 period with the AVHRR2 sensor, and (b) 2016 belongs to the 2001-2018 period with the AVHRR3 sensor. 29


	Fire_cci ATBD AVHRR-LTDR	Ref.:	Fire_cci_D2.1.3_ATBD-AVHRR-LTDR_v1.0		
		Issue	1.0	Date	19/11/2021
		Page	7		

Figure 12. Annual BA (Mkm²) trends of MCD64A1, FireCCI51, FireCCILT10 Beta and FireCCILT11. 41

Figure 13. Monthly median trends of the products: FireCCILT11, FireCCI51 and MCD64A1, in the common time series. 41

Figure 14. Annual BA trends of MCD64A1, FireCCI51 and FireCCILT11 in the different continental regions (year 1994 excluded). 44

Figure 15. Comparison of BA trends among national official perimeters and BA products (year 1994 excluded). 45

Figure 16. Comparison of BA trends among BA products in the US (year 1994 excluded). 46

Figure 17. Comparison between BA products using regional studies (year 1994 excluded). 46

Figure 18. Pareto boundary with a long-term Landsat dataset, which is resampled at low resolution and binarised in percentiles of proportions (green), FireCCILT11 binarised according with percentiles of proportion (blue) and FireCCILT11 (brown). 50

	Fire_cci ATBD AVHRR-LTDR	Ref.:	Fire_cci_D2.1.3_ATBD-AVHRR-LTDR_v1.0		
		Issue	1.0	Date	19/11/2021
		Page	8		

1 Introduction

1.1 Background

The ESA Fire_cci project focuses on developing and validating algorithms to meet GCOS ECV requirements for (consistent, stable, error-characterized) global satellite data products from multi-sensor data archives. Fire modellers require precise information on the timing, size, intensity and spatial distribution of fires (Hantson et al. 2016). Satellite burned area products have been generated in the last years based on existing global observation sensors (Mouillot et al. 2014), such as MODIS, VEGETATION, ATSR, MERIS, Sentinel-2 and Sentinel-3 data. These products only cover from 2000 and all show inconsistencies and omission and commission errors (Granier et al. 2011; Padilla et al. 2015). Most papers dealing with fire models emphasize the need to extend the existing time series of burned area information backwards. Although the GFEDv4 includes BA trends from 1995, the authors recognize greater uncertainties for the pre-MODIS era (Giglio et al. 2010). Estimations for previous periods were based on fire ignition and propagation models (Thonicke et al. 2001) or on fire occurrence reports provided by some national fire services (Mouillot and Field 2005). These data were complemented with auxiliary sources, such as journalist news, literature sources or charcoal deposits in lakes (Power et al. 2010).

The alternative to extend the BA datasets before the MODIS era was the NOAA-AVHRR (Advanced Very High Resolution Radiometer) archive, dated back to 1981. Unfortunately, only a degraded version of the AVHRR data was archived globally. It was named Global Area Coverage (GAC, at 4x4 km), obtained through a spatial sampling of the High Resolution data (HRPT, 1x1 km approximately at nadir). From the GAC data, NASA has released a time series of AVHRR data, which adequate calibrations and geometric, radiometric and atmospheric corrections to make it useful for time series analysis. Since the HRPT data were archived only at particular regions and needs considerable pre-processing effort, it was considered that the LTDR was the most adequate time series of AVHRR datasets to feed a BA algorithm that would extend the BA time series of the Fire_cci baseline contract.

FireCCILT10 Beta product was a first try to obtain a global long-term BA product. That product has several issues and problems such as inconsistency trends due to sensor degradation, and low BA detection in boreal and temperate regions. Although FireCCILT10 presented a good performance in tropical regions (Otón and Chuvieco 2018; Otón et al. 2019).

2 BA Algorithm description

2.1 General scheme

The methodology was based on several steps as seen in Figure 1. The structure and some steps have been obtained from FireCCILT10 algorithm (Otón and Chuvieco 2018; Otón et al. 2019) but the new algorithm (Otón et al. 2021b) has many novelties and improvements (Table 1). First of all, three inputs (Section 2.2) were still necessary to start the process: the AVHRR-LTDR product (version 5, Pedelty et al. 2007) from 1981 to 2018 (Section 2.2.1); land cover data (CCI and Copernicus Land Cover products) (Section 2.2.2). In the previous version, a single Land cover (year 2000) was used and now, a Land cover per year was used to achieve better adaptability to Land cover changes (burnable-unburnable). The last input, the BA product FireCCI51 (Lizundia-

	Fire_cci ATBD AVHRR-LTDR	Ref.: Fire_cci_D2.1.3_ATBD-AVHRR-LTDR_v1.0
		Issue 1.0 Date 19/11/2021
		Page 9

Loiola et al. 2020) (Section 2.2.3) was resampled to train the Random Forest (Breiman 2001) models instead of NASA MCD64A1 Collection 6 (MCD64A1 hereafter) BA product (Giglio et al. 2018), to improve the proportions of Burned Area and to increase the number of burned cases. Temporal composites (Section 2.3.1), Spectral Indices, Cloud Mask (Section 2.3.2) and a Burnable Mask were calculated to obtain LTDR Burned Index (LBI) (Section 2.3.3). Specifically, Cloud Mask calculation was significantly improved using more stringent conditions based on the literature. Yearly profiles select an immediate month even if they were from another year, instead of only the months within the natural year.

After processing data to prepare to train random forest (RF), which was improved with a new classification approach and parameters, two types of RF were developed (Section 2.3.4). One of them was a global RF model where global data enters, and a Boreal RF model where boreal data, more than latitude 49, was taking into account because it has a different signal response, number of samples and conditions, which in a global model were conditioned by tropical fires.

Henceforth, the processes were done for each type of model. RF results were obtained per month and global/boreal in probabilities which indicated the probability of a pixel to be burned or not. A new approach (Section 2.4) was undertaken where a formula per month and continental region (Giglio et al. 2013) was developed according to the Dice Coefficient (DC) sensitivity analysis (Section 2.4.1.1) from the last algorithm, Otsu thresholding (Otsu 1979) to adapt the threshold to each image (Section 2.4.1.2), and Solar Zenith Angle (SZA) correction (Section 2.4.1.3) to decrease the effect of sensor degradations and better detection of burned pixels. That formula was applied to each probability image to get a binary classification. A proportion analysis (Section 2.4.2) in the FireCCI51 time series per continental region was carried out to assign a proportion in the binary classifications. When BA proportions were assigned in the global and boreal results, both were joined in a single monthly classification to obtain a final BA product, called FireCCILT11.

Table 1. Changes in the BA algorithm from the FireCCILT10 Beta product.

	FireCCILT10	FireCCILT11
Input data		
Training data	MCD64A1 C6 product	FireCCI51 product
Land cover	A single LC in the time series (year 2000)	Annual (from 1992)
	ESA CCI-LC v1.6.1 product	ESA CCI-LC v2.0.7 product and C3S-LC v2.1.1 product.
Cloud mask	Red and NIR values > 90%	Criteria to filter clouds (Section 2.3.2)
Temporal sequence		
Yearly profiles	All months within a single year	Regressive and progressive months to contiguous months
Random Forest models		
# samples in each tree	20k	10M
Years to train	8 years	18 years
Models	Global	Global and boreal
Thresholding methods		
Monthly thresholding	Global for time series	Regional for each image
Adaptive thresholds	Dice Coefficient	Otsu method and Dice Coefficient

	Fire_cci ATBD AVHRR-LTDR		Ref.: Fire_cci_D2.1.3_ATBD-AVHRR-LTDR_v1.0	
			Issue 1.0	Date 19/11/2021
			Page 10	

	FireCCILT10	FireCCILT11
Input data		
SZA correction	Not applied	Regional for each image (1982-2000)
BA proportions		
Monthly BA assignments	Global	Regional
Cases (Figure 3)	A and B	The four cases
Products		
Years	1982-2017	1982-2018

Finally, the BA product was inter-compared (Annex 2: Inter-comparison) with other BA global products, national fire perimeters, regional BA products and other studies (Otón et al. 2021b), and was validated (Otón et al. 2021a) with Landsat perimeters (Annex 3: Validation) and a consistent low-resolution method (Pareto Boundary, Boschetti et al. 2004). A temporal trend analysis is described in Otón et al. (2021c).

This new product, called FireCCILT11, has been developed from 1982 to 2018 (no data available for 1994) and includes pixel and grid BA values on a monthly basis. The pixel and grid products are publicly available at: <https://climate.esa.int/>, last accessed in October 2021, or through the CCI Open Data Portal (<http://cci.esa.int/data>, last accessed in October 2021). Also, it is available in Google Earth Engine (https://code.earthengine.google.com/?asset=users/g_oton/FireCCILT11, last accessed on October 2021).

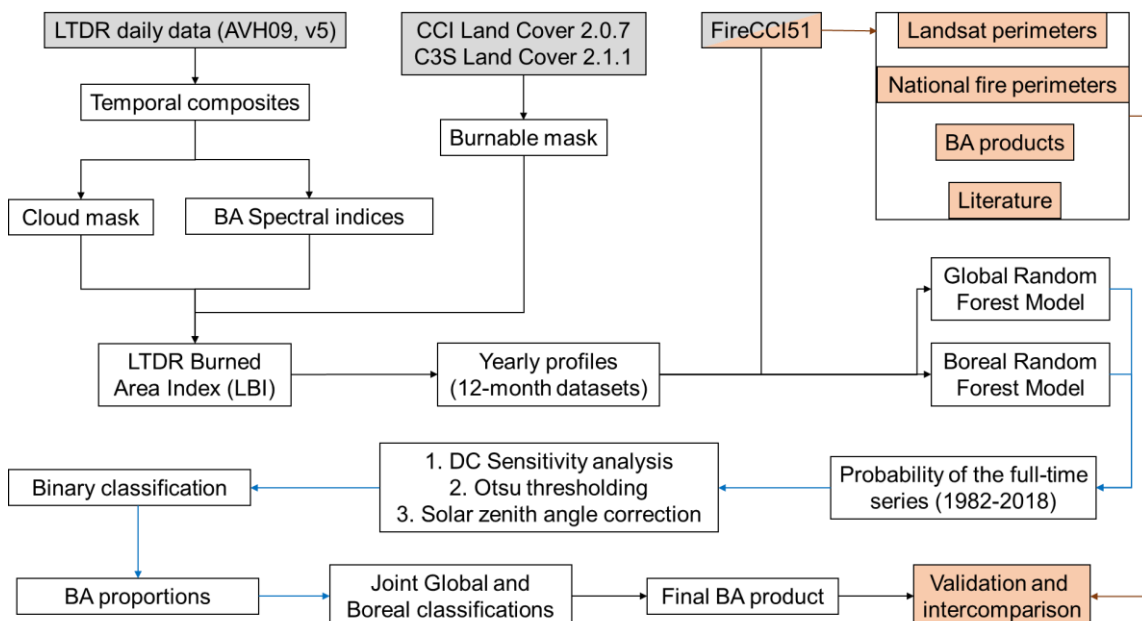


Figure 1. FireCCILT11 algorithm is shown as a flowchart. Gray boxes are the input data where the algorithm starts. Orange/beige boxes are data to compare and validate the new BA product. Black lines mean that the process is running once per month or year, blue lines that the process is running twice per month or year, one per each RF model. Orange/beige lines are validation and inter-comparison.

	Fire_cci ATBD AVHRR-LTDR	Ref.:	Fire_cci_D2.1.3_ATBD-AVHRR-LTDR_v1.0		
		Issue	1.0	Date	19/11/2021
		Page	11		

2.2 Input data

2.2.1 AVHRR-LTDR product

NASA created a global-full time series of AVHRR data, at 0.05° resolution (approx. 5 km), named the long-term data record (LTDR) dataset. There are various others long-term coarse AVHRR data series (GIMMS or Pathfinder), whose strengths and weaknesses have been cross validated, as reported in the literature (Alcaraz-Segura et al. 2010; Tucker et al. 2005). Taking into account those analysis, the AVHRR LTDR data series was chosen as the most adequate input for extending the Fire_cci BA datasets back to early 80's.

LTDR product (Version 5) is a long-term NASA dataset of satellite Earth observations (40 years) based on NOAA-AVHRR observations. It consists of only the afternoon (ascending) passes from the NOAA polar orbiting satellites. In particular, it is collected by NOAA-7, 9, 11, 14, 16, 18, and 19. The original data was acquired by the AVHRR 2 and 3 sensors and stored in reduced resolution, in Global Area Coverage (GAC, 4 x 4 km) images. GAC resolution is further reduced from the original resolution (Local Area Coverage [LAC], 1.1km, https://www.avl.class.noaa.gov/release/data_available/avhrr/index.htm#top, last accessed on October 2021) that was globally stored in 1991. LTDR is daily, global and resampled to 0.05° (~5 km), from 1981 to date, although the time series is not fully continued. There are a number of observational limitations, where the most important two were found in 1994 and from 2019 to date. 1994 presents important gaps and noise in the images from March and empty data from September, due to a satellite (N11) degradation (Otón et al. 2019; Riaño et al. 2007; Tucker et al. 2005) and lack of N13 (failed, Carmona-Moreno et al. 2005) supplied by N14 (Ignatov et al. 2004). From 2018 onwards the data quality from the satellite (N19) has been degrading, with important gaps in the images and noise, which makes the data unusable for obtaining acceptable results (https://www.usgs.gov/centers/eros/science/usgs-eros-archive-advanced-very-high-resolution-radiometer-avhrr?qt-science_center_objects=0#qt-science_center_objects, last accessed on October 2021). Consequently, 1994, 2019 and 2020 were not used (Hansen et al. 2018; Tian et al. 2015) in the development of the FireCCILT11 product.

The LTDR product has three products: AVH02 TOA Surface Reflectance Product, AVH09 Surface Reflectance Product and AVH13 NDVI Product. In this study, AVH09 is used, which is preprocessed and has ten original channels. The channels are surface reflectance for channel 1 (red, 0.58–0.68 µm) and channel 2 (near infrared, 0.725–1.1 µm), medium infrared (surface reflectance and top of atmosphere (TOA) brightness temperature for channel 3, 3.55–3.93 µm), and thermal infrared (TOA brightness temperature for channel 4, 10.3–11.3 µm and TOA brightness temperature for channel 5, 11.5–12.5 µm), view zenith angle, SZA, relative azimuth, and quality assessment field (QA).

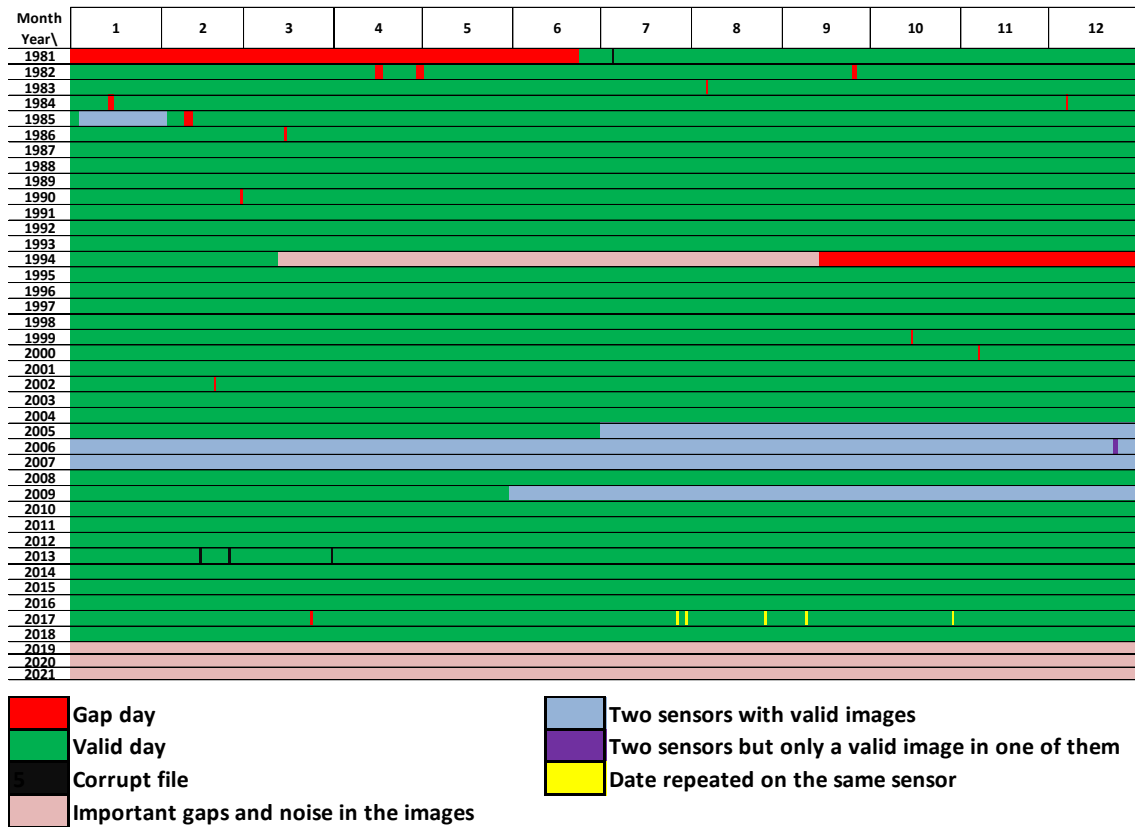


Figure 2: availability of LTDR v5.0 daily images for the full time series.

The AVHRR-LTDR V5 products for the 1981-2021 time period are:

- Surface reflectance:
 - SREFL_CH1 (0.58 – 0.68 μm)
 - SREFL_CH2 (0.725 – 1.1 μm)
 - SREFL_CH3 (3.55 – 3.93 μm)*
- TOA brightness temperature:
 - BT_CH3 (3.55 – 3.93 μm)*
 - BT_CH4 (10.3 – 11.3 μm)
 - BT_CH5 (11.5 – 12.5 μm)
- View zenith angle (VZEN), Solar zenith angle (SZEN according to LTDR product or SZA according to this document).
- Relative azimuth (RELAZ).
- Quality Assessment Field (QA).
- Fill value (No Data) = -9999
- Scale Factor:
 - Surface reflectance = 0.0001
 - TOA brightness temperature = 0.1
 - Zeniths and Azimuth = 0.01
- Spatial reference:
 - GCS datum based upon the Clarke 1866 ellipsoid.
 - EPSG: 4008
 - Datum: Based on Clarke 1866 spheroid
- Satellites (and sensors) used to generate the LTDR dataset are the following:
 - N07 (AVHRR2): 1981 – 1985
 - N09 (AVHRR2): 1985 – 1988

	Fire_cci ATBD AVHRR-LTDR		Ref.: Fire_cci_D2.1.3_ATBD-AVHRR-LTDR_v1.0	
			Issue 1.0	Date 19/11/2021
			Page 13	

- N11 (AVHRR2): 1988 – 1994
- N14 (AVHRR2): 1995 – 2000
- N16 (AVHRR3): 2000 – 2007
- N18 (AVHRR3): 2005 – 2009
- N19 (AVHRR3): 2009 – 2021

(*) From 2000 to 2003, the channel 3 was changed from 3.55 – 3.93 μm to 1.58 - 1.64 μm for day time acquisitions.

Several corrections and calibrations have been applied based on the Pathfinder program (El Saleous et al. 2000). Among the corrections, there are radiometric, geometric and atmospheric corrections (Rayleigh scattering, ozone, water vapour, and aerosol correction such as aerosol correction in Pinatubo and El Chinchon eruptions (El Saleous et al. 2000; Vermote et al. 2009)), and BRDF correction by MODIS (Villaescusa-Nadal et al. 2019b). Furthermore, the LTDR dataset take into account several calibrations, where the visible and near infrared were empirically calibrated, due to the lack of any onboard calibration in the satellite (El Saleous et al. 2000), and the multisensory calibration using spectral adjustment selecting N14 as a reference (Villaescusa-Nadal et al. 2019a). Infrared channels are calibrated onboard.

Despite this, some inconsistencies (Beck et al. 2011; Otón et al. 2019) are present in the visible channels due to degradation in the sensors, and the entrance of new AVHRR sensors which destabilize the time series. The reconfiguration of Channel 3 (from 3.55–3.93 μm to 1.58–1.64 μm) over 3 years and the different saturation of Channel 3 between AVHRR2 (50°C) and AVHRR3 (63°C) (Otón et al. 2019; Trishchenko et al. 2002) make that Channel inconsistent for use in the algorithm (Otón et al. 2019). Furthermore, the degradation of the sensors implies severe orbital drift (Figure 2) from Sun-synchronism (Csiszar et al. 2003; McGregor and Gorman 1994; Price 1991; Riaño et al. 2007; Weber and Wunderle 2019), they lack an orbit adjust system to compensate for varying atmospheric drag (Price 1991), which produces a delay upon the cross the equator (Privette et al. 1995) and provokes variations of illumination (Csiszar et al. 2003; McGregor and Gorman 1994; Privette et al. 1995; Riaño et al. 2007; Weber and Wunderle 2019), different diurnal cycle (Ignatov et al. 2004), false trends, changes in background temperatures (measured reflectance and brightness temperatures, Weber and Wunderle 2019), signal properties (Tian et al. 2015) and poor quality of data (Otón et al. 2019). These variations and problems are greater when the SZA are higher (Stengel et al. 2020). Therefore, the sensor degradation is recognized as being of about $\approx 5\text{-}10\%$ in the relative accuracy of the visible channels (Los et al. 1994).

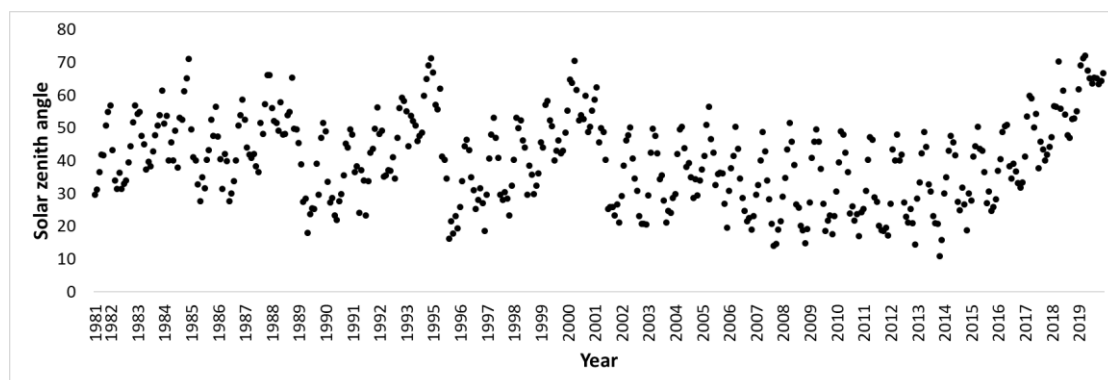


Figure 3. Time series of solar zenith angle values for a stable pixel located in Sahara Desert - Mauritania (20.35°N, -8.3°W) - of the LTDR time series. The impact of sensor's degradation produces a delay in the cross the pixel.

	Fire_cci ATBD AVHRR-LTDR		Ref.: Fire_cci_D2.1.3_ATBD-AVHRR-LTDR_v1.0	
			Issue 1.0	Date 19/11/2021
			Page 14	

Moreover, high latitudes have lacks and low quality of observations in winter in both hemispheres (Otón et al. 2019), because the satellites cover those latitudes at night (Giglio and Roy 2020).

The LTDR product, although with some issues yet to improve, is a useful and important dataset. In fact, it has been used in different studies such as Vegetation Continuous Fields (Hansen et al. 2018), surface phenology (Zhang et al. 2014) and BA detection (García-Lázaro et al. 2018; Moreno-Ruiz et al. 2019; Otón et al. 2019).

2.2.2 Land Cover

ESA's CCI Land Cover v2.0.7 (CCI-LC, ESA 2013) product and Copernicus Climate Change Service (C3S) Global Land Cover (C3S-LC, Copernicus 2019) products v2.1.1 are global and annual Land Cover products to 300m of spatial resolution. CCI-LC products were developed within the CCI programme (<https://climate.esa.int/en/projects/land-cover/>, last accessed on October 2021) from 1992 to 2015 and C3S-LC (<https://cds.climate.copernicus.eu/>, last accessed on October 2021) from 2016 to 2019. This last product aims to be the continuation of the CCI-LC product and is fully consistent with its predecessor, keeping a similar temporal and spatial resolution that allows their use in the algorithm. Both products were used to generate a burnable mask (Otón et al. 2019), to optimize the algorithm and avoid probable commission errors, reclassifying (burnable and unburnable) and resampling to the AVH09 resolution (0.05 degrees). Unburnable areas were bare soil, water, urban areas, permanent snow and ice (Otón et al. 2019, Lizundia-Loiola et al. 2020). After that process, we obtained the burnable proportion area within each pixel. In the case that the burnable proportion area in a pixel was lower than 20%, that pixel was discarded from the analysis (Otón et al. 2019; Plank et al. 2017). We selected the previous year to the study year to take into account the cover conditions and variability of the target period. For the 1982-1992 period, land cover from 1992 was used as CCI and C3S don't provide information before 1992.

2.2.3 FireCCI51

The FireCCI51 dataset (Lizundia-Loiola et al. 2020) is a global BA product developed within the CCI programme (<https://climate.esa.int/en/projects/fire/>, last accessed on October 2021). Its use keep consistency with the CCI programme. That product is generated through MODIS images from its first date of availability (from 2001 to 2020) and also uses the CCI-LC. FireCCI51 is a global and monthly dataset at 250m in the pixel product and 0.25° in the grid product. It has been validated using a global statistical design sample, showing similar accuracy to other global BA products (commission error (Ce) = 54.4%, omission error (Oe) =67.1%), although that product has shown to be more sensitive in detecting smaller burned patches (Lizundia-Loiola et al. 2020, Moreno-Ruiz et al. 2020) than MCD64A1. Furthermore, FireCCI51 increases the number of burned cases noticeably. FireCCI51 detects a 10% more BA than MCD64A1 globally, and increases BA in most continental regions (10 of 14) of the world. Significantly, FireCCI51 detects more BA (up to ≈75%) in boreal and template regions of Europe and Asia. FireCCI51 also shows a good performance in Boreal America region (Moreno-Ruiz et al. 2020), being better than MCD64A1. Therefore, that product in pixel format was resampled at 0.05° to for use it in the algorithm.

2.3 Pre-processing of LTDR data

2.3.1 Composites

Composite techniques are a suitable and frequent method for improving the utility and quality of daily data in time series analysis (Roy 1997). Thereby, those techniques can smooth or remove clouds, shadows, noise, radiometric instability, very oblique angles or artefacts, depending on the chosen method, which underestimate biophysical parameter values (Los et al. 1994). In this study, we created monthly composites, usually used in BA (Chuvieco et al. 2018; Giglio et al. 2013; Grégoire et al. 2003; Lizundia-Loiola et al. 2020), or long-term studies (Hansen et al. 2018; Tian et al. 2015), from the AVH09 product. In particular, we selected the maximum temperature technique (MaxT) which offered robustness and great results in several studies. That technique increases atmospheric attenuation and sensitivity to the detection of burned pixels, but decreasing or avoiding clouds, cloud shadows, high satellite zenith angle and off-nadir pixels (Cihlar et al. 1994; Chuvieco et al. 2005; Roy 1997). Between two temperature channels in AVH09, channel 4 (10.3–11.3 μm) was chosen because it has a stable calibration (Cihlar et al. 1994), high saturation (57°C), and deletes high and cold clouds (Li et al. 2001).

2.3.2 Cloud Masking

In the development of BA products it is essential to provide cloud-free images to the algorithm (Giglio et al. 2018; Lizundia-Loiola et al. 2020). AVH09 QA is not accurate (Otón et al. 2019) and MaxT composites eliminated a great number of affected pixels but clouds were able to be present for various reasons, for example: that all observations were cloudy in a pixel when the composite was created, or that difficult clouds to remove with Channel 4 such as low clouds (Li et al. 2001). There are many cloud mask studies available (James and Kalluri 1994; Simon et al. 2004; Stroppiana et al. 2002) although in our case, most interesting approaches were global studies (James and Kalluri 1994; Tucker et al. 2005). We have mixed some interesting methodologies to adjust them to our available data and features (Table 2). We have created a threshold method to detect cloud-free pixels, where Channel 1 reflectivity of more than 40% is removed (Stroppiana et al. 2002) to delete low clouds and fire smoke (Li et al. 2001); albedo (Channel 1 divided by Channel 2) more than or equal to 0.9 and albedo less than or equal to 1.1 was removed to eliminate reflectance ratio clouds (James and Kalluri 1994); Channel 4 less than 249K ($\approx -24^\circ\text{C}$) was removed to delete thermal gross clouds (James and Kalluri 1994), high and cold clouds (Li et al. 2001); and Channel 5 less than 273K ($\approx 0^\circ\text{C}$) was removed to eliminate cloud screening (Tucker et al. 2005).

Table 2. Criteria to filter clouds in the AVH09 images. If one of the conditions is met, the pixel is filtered.

Criteria	Description	Reference
Channel 1 $\geq 40\%$ reflectance	delete low clouds and fire smoke	Stroppiana et al. (2002)
$0.9 < \text{Albedo} < 1.1$ Where: $\text{Albedo} = \frac{\text{Channel 1}}{\text{Channel 2}}$	eliminate reflectance ratio clouds	James and Kalluri (1994)
Channel 4 $\leq 249\text{K}$	delete thermal gross clouds, high and cold clouds	James and Kalluri (1994)
Channel 5 $\leq 273\text{K}$	cloud screening	Tucker et al. (2005)

	Fire_cci ATBD AVHRR-LTDR	Ref.:	Fire_cci_D2.1.3_ATBD-AVHRR-LTDR_v1.0		
		Issue	1.0	Date	19/11/2021
		Page	16		

The number of observations was calculated monthly as the sum of the daily observations (0-28/31) in which a pixel follows the No cloud mask conditions. If there were two satellites available, the number was divided into two to keep the coherence throughout the time series.

2.3.3 LTDR Burned Index (LBI)

Input bands of LTDR Burned Index (LBI) were obtained by a statistical analysis in Otón et al. (2019). In that study several original bands, common spectral indices and monthly temporal differences were analysed in a spectral BA separability study. The most sensitive variables to discrimination between burned and unburned pixels were selected. These variables are very common in BA studies: Channel 1 (0.58–0.68 μm) or Red (Chuvienco et al. 2018; Moreno-Ruiz et al. 2012; Plank and Martinis 2018; Ramo and Chuvienco 2017), Channel 2 (0.725–1.1 μm) or NIR (Chuvienco et al. 2008; Lizundia-Loiola et al. 2020; Moreno-Ruiz et al. 2013; Moreno-Ruiz et al. 2012; Plank and Martinis 2018; Ramo and Chuvienco 2017), Channel 5 (11.5–12.5 μm) or T5 (Plank et al. 2017), Global Environmental Monitoring Index or GEMI by Pinty and Verstraete (1992) (Carmona-Moreno et al. 2005; Chuvienco et al. 2008; Chuvienco et al. 2018; Moreno-Ruiz et al. 2013; Moreno-Ruiz et al. 2012; Oliva et al. 2011; Riaño et al. 2007), Burned Area Index or BAI by Chuvienco et al. (2002) (Chuvienco et al. 2008; Long et al. 2018; Plank and Martinis 2018) and temporal differences (Bastarrika et al. 2018; Dillon et al. 2011; Fraser et al. 2000; Li et al. 2001; Moreno-Ruiz et al. 2013; Plank and Martinis 2018; Vhengani et al. 2015), the latter being very important in any product (Giglio et al. 2018; Lizundia-Loiola et al. 2020).

$$\text{GEMI} = \eta \cdot (1 - 0,25 \cdot \eta) - \left(\frac{\rho_{RED} - 0,125}{1 - \rho_{RED}} \right) \quad (1)$$

$$\eta = \frac{(2 \cdot (\rho_{NIR}^2 - \rho_{RED}^2) + 1,5 \cdot \rho_{NIR} + 0,5 \cdot \rho_{RED})}{\rho_{NIR} + \rho_{RED} + 0,5} \quad (2)$$

$$\text{BAI} = \frac{1}{(\rho_{CRED} - \rho_{RED})^2 + (\rho_{CNIR} - \rho_{NIR})^2} \quad (3)$$

Where ρ_{NIR} and ρ_{RED} are the reflectance values of the NIR and Red channels, respectively, and ρ_{CNIR} and ρ_{CRED} are the convergence values for burned vegetation (defined for AVHRR by the authors of the index as 0.06 and 0.1, respectively).

To increase the consistency of the temporal series, the variables (X) were normalized (z-score):

$$z = \frac{X - \mu}{\sigma} \quad (4)$$

where μ and σ are the mean and the standard deviations of the values of each monthly composite and X is the value in the month.

The LBI formula was:

$$\text{LBI} = z(T5) - z(T5_diff) - z(Red) + z(Red_diff) - z(NIR) + z(NIR_diff) + z(GEMI) + z(BAI) + z(BAI_{t+1}) \quad (5)$$

	Fire_cci ATBD AVHRR-LTDR		Ref.:	Fire_cci_D2.1.3_ATBD-AVHRR-LTDR_v1.0		
			Issue	1.0	Date	19/11/2021
			Page			17

(please note that the original definition of Otón et al. (2019) had an error that was later on noticed (Otón et al. 2020)).

What in the formulas is called “diff” represents the difference between the composite of the month being analysed (t) and the composite of the previous month (t-1). Thus, t+1 is the composite of the following month.

LBI were computed for each monthly composite. LBI shows the burned likelihood in a pixel, which present a positive strong response about the burned date, maximizing the spectral separation between burned and unburned pixels and facilitating the classification process. Since the LBI included a normalization of the temporal series, it was expected to be less sensitive than the original bands to variations in the SZA, particularly in the thermal channels. We checked (Table 3) this correction in a stable place with spatial uniformity (Cosnefroy et al. 1996) of the Algerian desert (23.80°N, 0.40°W, Giglio and Roy 2020). The input of spectral indices (BAI and GEMI) and the LBI itself strongly reduced the impact of SZA and its consequences as also shown NDVI in other studies (Kaufmann et al. 2000; Los et al. 1994).

Table 3. Correlation analysis between the Algerian desert pixel (23.80°N, 0.40°W) of the different variables of the synthetic index and LBI. The Pearson’s r is calculated for the time series of the study and for the AVHRR2 (1982-2000) and the AVHRR3 (2001-2018) period.

	Channel 1	Channel 2	Channel 5	GEMI	BAI	LBI
1982-2018	-0,022	0,068	-0,837	0,062	0,045	0,043
1982-2000	0,056	0,043	-0,812	-0,053	0,002	0,010
2001-2018	0,022	0,034	-0,874	-0,057	0,081	-0,073

2.3.4 Burned area detection models

Machine learning is a powerful tool used in multitude of studies but that does not mean that it is the solution to all problems or questions (Jain et al. 2020). The most outstanding classifiers are Random Forest (RF), Super Vector Machine (SVM) or Neural Network (NN). SVM and NN are robust but more complex than RF (Rodriguez-Galiano and Chica-Rivas 2012). RF was developed by Breiman (2001) and is the most accurate and robust methodology in several comparisons reviewed (Ramo et al. 2018; Rodriguez-Galiano et al. 2015; Rodriguez-Galiano and Chica-Rivas 2012). In RF the amount of training data does not matter, and it only needs a few parameter settings (Rodriguez-Galiano et al. 2015; Rodriguez-Galiano and Chica-Rivas 2012). RF is based on a decision trees combination, simpler methodology already used in fire studies such as classification (Dubinin et al. 2010) or regression models (Giglio et al. 2010; Hansen et al. 2018). RF classifications have been trained in many studies and diverse thematic, for example: mineral prospective (Rodriguez-Galiano et al. 2015), land cover (Rodriguez-Galiano et al. 2012), BA severity (Dillon et al. 2011) and BA (Ramo and Chuvieco 2017); less often we can see RF regression (Bunn and Goetz 2006).

The databases were composed of all the years (2001-2018, 18 years) available, in which there were MODIS BA (FireCCI51) product to reduce noise input, as did Villaescusa-Nadal et al. (2019b) by introducing 15 years into their BRDF study. Monthly databases were created to adjust the conditions of fire per each month, similar to Dillon et al. (2011) where they differentiated between ordinary years or not. As happens in different studies, few variables were entered (Dillon et al. 2011; Ramo and Chuvieco 2017; Rodriguez-Galiano et al. 2012). FireCCI51 grid cell was used to train the RF model

where two classes (burned/unburned) are differentiated, being burned (any BA proportion). 75% of database entered in the classification and 25% in the validation.

RF parameters (Section 2.3.4.1) are redefined and run in Scikit-learn (Pedregosa et al. 2011). We conserved the trees number at six hundred (Otón et al. 2019; Ramo et al. 2018) for its good precision-time relation, and we assigned a weight of 10% because our database is unbalanced (most data are burned) and burned data acquired more value in the context (Otón et al. 2019; Ramo et al. 2018). The maximum depth of the tree is expanded with all its leaves since pruning it does not prevent possible overtraining (Rodríguez-Galiano et al. 2012). Each tree is trained with ten million samples selected randomly. The RF outcomes were probabilities.

The most important novelty regarding the beta version (Otón et al. 2019) was the development of two types of databases, one global and the another boreal. Despite RF being automatic and not needing local adaptation, it may not work the same spatially (Ramo and Chuvieco 2017). Due to different spatial accuracy and the gaps in the beta version, we decided to add a boreal model. This was partly caused by the differences between Boreal and Tropical fires, and the larger impact of the latter in generating global models (as most worldwide burned area occurs in Tropical regions (Dwyer et al. 2000; Melchiorre and Boschetti 2018).

Therefore, two types of monthly databases (Figure 4) were developed to train global and boreal monthly RF models. In the temporal aggregation, global databases contained twelve months of LBI, while for boreal databases contained eight (March-October) as the probability of having Boreal fires in winter is very low (Beck et al. 2011; Kucêra et al. 2005), to include a complete temporal evolution of pre- and post-fire conditions. These monthly databases were generated by using five or three months previous to the burned one (auto-regressive months, Riaño et al. 2007), and the six or four months next to the burned one (auto-progressive months) depending on the type of model (global or boreal, respectively).

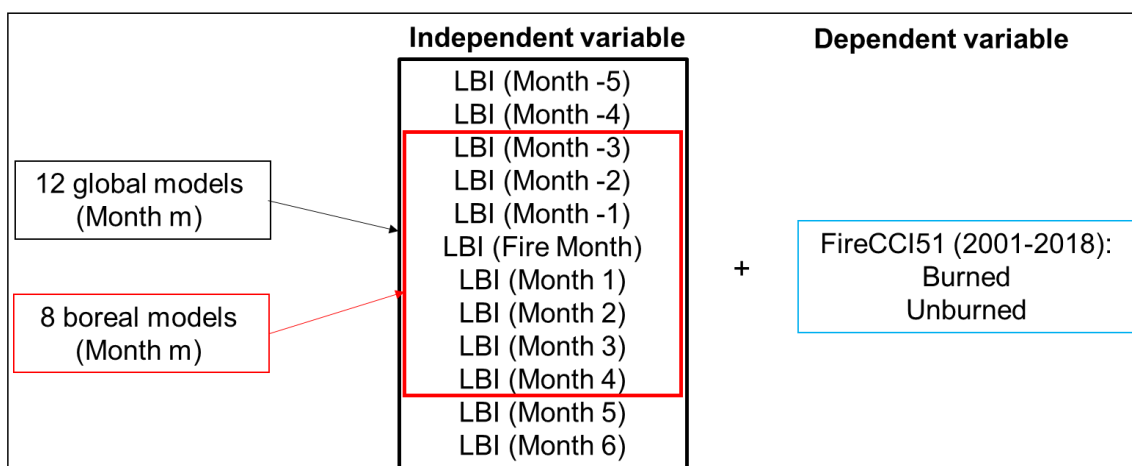


Figure 4. Monthly composites used to create the RF models. Monthly models were created using LBI values from several months before and after the target period. For instance, the global RF model of August had as independent variables the LBI of August, LBI of five months before August (that is, March to July) and LBI of six successive months (September to February). The dependent variable was the target BA (FireCCI51) of each target month, in this example was the FireCCI51 of August. For the Boreal model winter months were discarded.

	Fire_cci ATBD AVHRR-LTDR		Ref.:	Fire_cci_D2.1.3_ATBD-AVHRR-LTDR_v1.0		
			Issue	1.0	Date	19/11/2021
			Page			19

Finally, RF classifications are run (720 times, 432 global and 288 boreal) with the twenty models for the whole time series (1982-2018, except 1994) to obtain the output (probabilities) which is also used by Long et al. (2018) and Otón et al. (2019).

RF probability is offered as the confidence level of the BA detection in the Pixel product and Standard error is calculated for the Grid product, which are available as auxiliary variables of the final FireCCILT11 product.

2.3.4.1 Random Forest parameter tests

The parameters were based on our previous experience (Otón et al. 2019), new tests and literature results (Ramo et al. 2018). We analyzed different models (new tests) and chose the best performances, according to:

- Number of samples in each tree (20k, 0.5M, 1M, 3M, 7M, **10M**, 11M (computational limit)) (Figure 5),
- Weight of the burn class (None, **10%**, 50%, Balanced) (Figure 6),
- Maximum depth of the trees (5, 10, 20, **None**) (Figure 7),
- FireCCI51 years to train (8, 15, **18**) (Figure 8),
- % of database to train the model (95%, 90%, **75%**) (Figure 8).

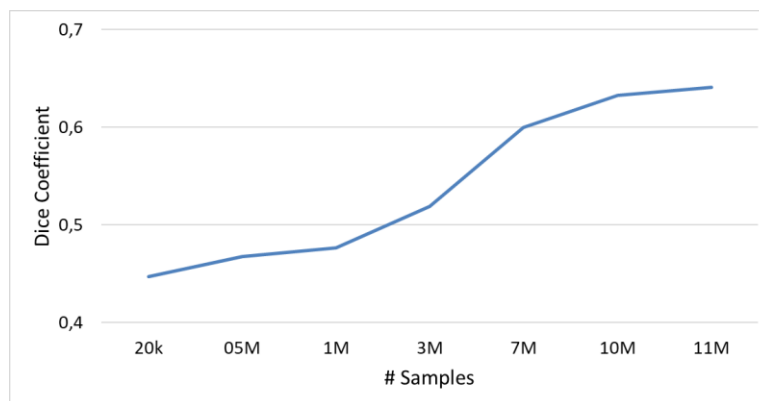


Figure 5. Analysis to obtain the best number of samples in each tree according to Dice Coefficient in the time series 2001-2018. From 20k used in FireCCILT10 Beta version to 11M which is our computational limit. 10M was selected in FireCCILT11, due to its accurate/time relation.

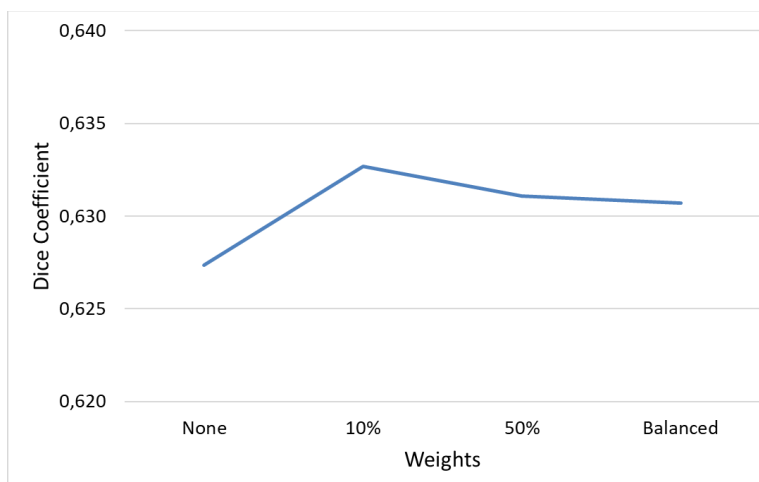


Figure 6. Analysis to obtain the weight assigned to the burn class according to Dice Coefficient in the time series 2001-2018. From no weight to Balanced. 10% was used in FireCCILT11 and FireCCILT10 Beta version where it was set up in a similar parameter.

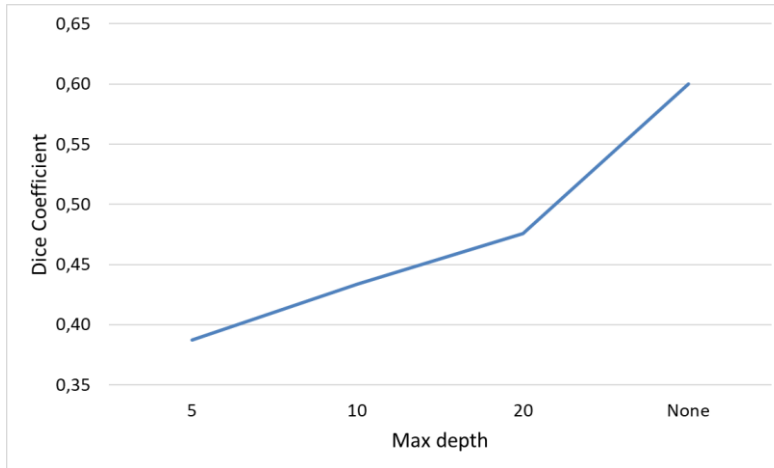


Figure 7. Analysis to obtain the maximum depth of the trees according to Dice Coefficient in the time series 2001-2018. From 5 to None. None was used in FireCCILT10 Beta version and FireCCILT11.

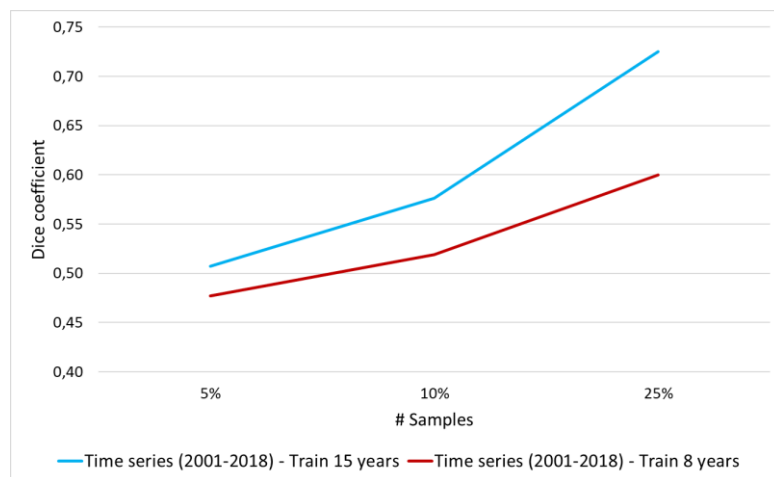


Figure 8. Analysis to obtain the years and the % of database to train the model according to Dice Coefficient. From 5% to 25% of samples to validate and 8 to 15 years to train the model. 10% and 8 years was used in FireCCILT10 Beta version and 25% and 18 years in FireCCILT11.

2.3.4.2 Spatial nature of fire events

Spatial coherence is common in the development of other algorithms (Giglio et al. 2010; Grégoire et al. 2003; Lizundia-Loiola et al. 2020; Moreno-Ruiz et al. 2013) since it reduces omission errors (Lizundia-Loiola et al. 2020), for example Moreno-Ruiz et al. (2013) divided the Boreal American region into six parts. Furthermore, there are many factors that bear out that decision, the signal of boreal regions can remain detectable from 2 to 3 years after-burning (Eurasia, Dubinin et al. 2010) to 6-9 years (America, Moreno-Ruiz et al. 2013) depending on the biomass, vegetation, location, levels of burning and size (Dwyer et al. 2000; Melchiorre and Boschetti 2018). Boreal fires are larger than other fires (Moreno-Ruiz et al. 2013). However, in other regions, the signal does not remain for so long (Melchiorre and Boschetti 2018), such as Africa where the signal decreases after 17 days (Eva and Lambin 1998). The boreal model took into account latitudes more than or equal to 49° (Figure 9) since the entrance of template regions decreased but most boreal places were conserved. Thereby, boreal signal was stronger and it was more adjusted to fire season. We only inserted the boreal fire season (Dubinin et al. 2010) in the boreal models from March to October as in other studies

(Beck et al. 2011; Kucêra et al. 2005). Some studies were stricter in selecting the growing season (May to August, Bunn and Goetz 2006) or the most burned months (April to September, Dubinin et al. 2010; Moreno-Ruiz et al. 2013), but we preferred more data variability.

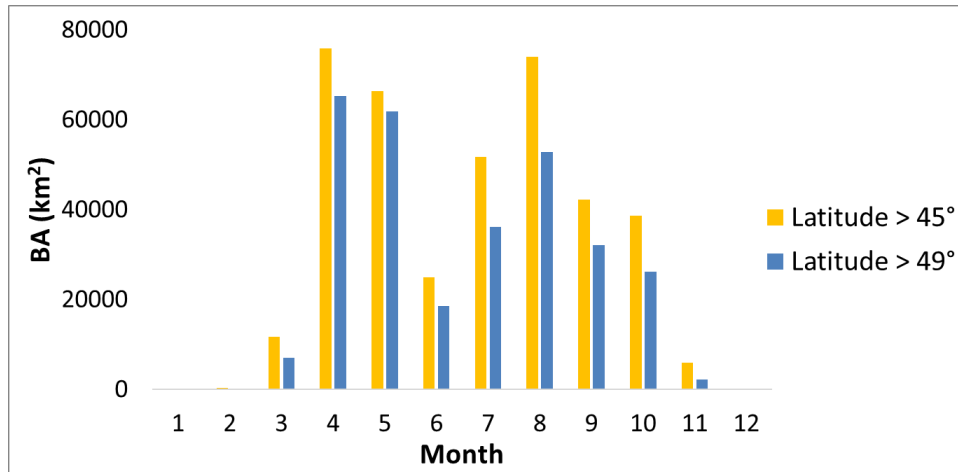


Figure 9. FireCCI51 BA average (2001-2018) per months according to high latitudes.

2.3.4.3 Global and boreal databases

In addition, the quantity of data was very significant between global and boreal. In a month with high BA data like August, we found around seventy-five million (75M-NBA global) of unburned samples in the global database (18 years) and half (around thirty-three million, 33M-NBA boreal) in the boreal database, but there were two million (2M-BA global) of BA in the global database and only 10% of BA (200k-BA boreal) in the boreal database. That difference was enormous for the correct training of a classification in RF, where there were other stronger signals of BA. Therefore, twenty models were done (Figure 4), twelve global models (one per month) and eight boreal models (one per month from March to October).

2.4 Post-processing of model probabilities

2.4.1 Binary classifications and Solar zenith angle correction

Probabilities (between 0.000 and 1.000) of a pixel to be burned or unburned were obtained from RF. Defining a threshold is necessary in order to find a correct point where the classification is accurate and the omission and commission errors are decreased. An adaptative, automatic and regional threshold is developed per each month and continental region (Giglio et al. 2013) for each one of the probabilities images. The adaptative threshold was based on:

- A fixed threshold, one per month and continental region but the same for the times series, obtained by a sensitive analysis of Dice coefficient.
- An automatic threshold, one per month and continental region in each probability image, from an Otsu regional thresholding.
- SZA correction, one per each probability image, month and continental region, by a SZA analysis.

Temporal and automatic thresholds (Barbosa et al. 1999; Riaño et al. 2007) are very common to cope with large amounts of data. Also, adaptative thresholds are common in

	Fire_cci ATBD AVHRR-LTDR	Ref.:	Fire_cci_D2.1.3_ATBD-AVHRR-LTDR_v1.0		
		Issue	1.0	Date	19/11/2021
		Page	22		

other algorithms to deal with different vegetation covers (Lizundia-Loiola et al. 2020), so they can adapt to the diversity of several conditions instead of applying only one threshold (Alonso-Canas and Chuvieco 2015; Chuvieco et al. 2018; Lizundia-Loiola et al. 2020; Plank and Martinis 2018). In the same way, in order to focus the separability in specific locations, regional thresholds (Fraser et al. 2000; Pu et al. 2018), local adaptive thresholds (Fraser et al. 2004; Giglio et al. 2010), relative thresholds (Moreno-Ruiz et al. 2013) and vicinity filters (García-Lázaro et al. 2018) are very often used.

2.4.1.1 DC sensitivity analysis


The best thresholds to convert the RF probabilities into a dichotomous classification (burned-unburned) in the FireCCI51 period were achieved by a sensitivity analysis. Thresholds between 0.00 and 1.00 (steps of 0.01) were iterated and the one with the classification more adjusted to FireCCI51 with the highest Dice Coefficient (DC) was chosen. The statistical DC (Dice 1945) is commonly used in BA studies (Lizundia-Loiola et al. 2020; Padilla et al. 2017; Padilla et al. 2015), as it incorporates both the omission and commission error of the BA class. A threshold was calculated per month and continental region of each image in the FireCCI51 time series (2001-2018), considering any percentage of BA as burned pixel. A median value (Med) per month was calculated using all the thresholds of the 2001-2018 time-series (with existing FireCCI51 data) to obtain the $Med(Threshold_{DC})$. This meant that these values were only suitable for the MODIS era, but may not be well adjusted to the remaining years. A possible slight overtraining in the training period (2001-2018) could cause that the probabilities be higher in the 2001-2018 period than in the 1982-2000 one. In addition, the signal between AVHRR2 and AVHRR3 can affect the results in the same way, making the probabilities of 1982-2000 weaker. Despite that, DC thresholds were useful, but they needed to be adjusted to each image.

2.4.1.2 Otsu threshold

An automatic threshold method was used to achieve a threshold that fits each of the images and each of the continental regions. Otsu method (Otsu 1979) is a non-parametric and automatic threshold selection without a parameter control. Otsu advantages are its simplicity, speed, efficiency, stability and universality (Zhan and Zhang 2019) and can be divided into global or local thresholding (Kumar and Tiwari 2019). The threshold achieved by Otsu has a spectral contrast power and maximizes the separability of two classes by a grey-level histogram. Otsu is designed to find a valley between two peaks in the histogram to separate two classes where the deeper point is the optimum threshold (Otsu 1979). Therefore, the optimum threshold is the minimum intra-class variance and the maximum inter-class variance (Bastarrika et al. 2018; Bin et al. 2019; Vijay and Patil 2016). Otsu thresholding is a technique widely used and modified in many studies to discriminate classes in images (Kittler and Illingworth 1985; Kumar and Tiwari 2019; Qu and Zhang 2010; Vala and Baxi 2013) such as mineral segments (Unajan et al. 2019; Zhan and Zhang 2019), changes detection (Huang et al. 2015) or BA (Amos et al. 2019; Bastarrika et al. 2018; Bin et al. 2019; Brown et al. 2018; Plank and Martinis 2018; Vhengani et al. 2015).

Despite its advantages, Otsu's method has general limitations, especially when the following situations occur:

1. Unclear separation in the valley of the histogram (Bastarrika et al. 2018),

	Fire_cci ATBD AVHRR-LTDR	Ref.:	Fire_cci_D2.1.3_ATBD-AVHRR-LTDR_v1.0		
		Issue	1.0	Date	19/11/2021
		Page	23		

2. Unbalance between target (burned) amount of pixels and not-burned pixels (Bastarrika et al. 2018; Kittler and Illingworth 1985; Unajan et al. 2019; Vala and Baxi 2013),
3. Discontinuous images (Qu and Zhang 2010), or
4. Image noise (Huang et al. 2015).

In those limitations, there would take place a worse separation of classes, and the missing of weak signals of the object class (Kumar and Tiwari 2019). In the case of BA studies, Otsu can underestimate BA (Plank and Martinis 2018), although in our case Otsu underestimated in regions and months with high fire occurrence such as the fire season of Africa, and overestimated (limitation 2) in regions and months with low fire occurrence like months out of the fire season or boreal regions.

Again, a median per month and continental region was calculated to obtain Med(Threshold_{Otsu}) for the period 2001-2018. Therefore, Otsu is adjusted by DC thresholds per month and continental region. Thereby, a relative constant is calculated in the 2001-2018 period (Med(Threshold_{DC})) per month, to learn how much correction is necessary in the Threshold_{Otsu} (according to each month from 2001-2018), so that corrected Otsu has values close to the optimal DC threshold, adapted to each image and region.

$$Relative\ constant_{m,CR} = \frac{Med(Threshold_{DC})_{m,CR}}{Med(Threshold_{Otsu})_{m,CR}} \quad (6)$$

In this way, we adjust the optimum Otsu threshold of each image to the Optimum DC threshold:


$$Corrected\ Otsu_{m,CR} = Threshold_{Otsu,m,CR} * Relative\ constant_{m,CR} \quad (7)$$

where m is the month, and CR is each of the continental regions. In this way, the corrected Otsu threshold has values close to the optimal DC threshold, but adapted to each image and region.

Accordingly, the under/over-estimation of Otsu threshold was corrected and the images maintain their variability.

In the case of continental region 1 or BONA (RF boreal model), it was necessary to do a regional correction due to the second Otsu limitation. In the central and eastern parts of that boreal region, the thresholds inserted a great deal of noise because there were many unburned pixels and few burned. Then, the Threshold_{Otsu} and later the Corrected Otsu thresholds were very low and did not offer a good separation of classes, resulting in large errors. That error only occurred in the 1982-2000 period where the thresholds were lower and did not happen in every year. Furthermore, the error, which was corrected, was concentrated in the fire season with the most fires (June-September). An Med(Threshold_{Otsu}) (June-September) between the 2001-2018 period was compared to the Threshold_{Otsu} (June-September) of the different years of the 1982-2000 period. If the values were differentiated less than by 35%, the relative constant was not applied to Otsu because there were values in the fire season higher than or equal to the train years; if the difference was between 35-50%, the usual Otsu correction was applied; and when the difference was more than 50%, the relative constant was elevated to the second power in the Otsu correction.

If median threshold difference < 35%:

	Fire_cci ATBD AVHRR-LTDR	Ref.: Fire_cci_D2.1.3_ATBD-AVHRR-LTDR_v1.0
		Issue 1.0 Date 19/11/2021
		Page 24

$$\text{Corrected Otsu}_{m,CR} = \text{Threshold}_{Otsu,m,CR} \quad (7.1)$$

If median threshold between 35-50%:

$$\text{Corrected Otsu}_{m,CR} = \text{Threshold}_{Otsu,m,CR} * \text{Relative constant}_{m,CR} \quad (7.2)$$

If median threshold > 50%:

$$\text{Corrected Otsu}_{m,CR} = \text{Threshold}_{Otsu,m,CR} * (\text{Relative constant}_{m,CR})^2 \quad (7.3)$$

On the one hand, the high thresholds did not lose their signal and they did not create omission. On the other hand, the low thresholds were increased, the noise was removed and the commission error was avoided. This type of adjustment has been performed in other boreal studies with other statistics like standard error (Kucêra et al. 2005).

2.4.1.3 Solar Zenith Angle correction

SZA is the angle between the solar centre and the zenith (the vertical) (Ji and Brown 2017; Privette et al. 1995). The SZA effect has been detected from the first satellites in orbit (McGregor and Gorman 1994). Several studies have advised of the orbital drift (Carmona-Moreno et al. 2005; Giglio 2007; McGregor and Gorman 1994; Price 1991; Privette et al. 1995; Weber and Wunderle 2019) but there are many uncertainties (Carmona-Moreno et al. 2005), and there is no standard correction yet. Orbital drift provokes a later satellite passing through the local solar times which gradually accelerates during the satellite's life (Carmona-Moreno et al. 2005; Devasthale et al. 2012; Ji and Brown 2017), Price (1991) observed 1-2h of delay, McGregor and Gorman (1994) around 3h, Carmona-Moreno et al. (2005) 2 h 30 min, Giglio (2007) 3–6 h and Weber and Wunderle (2019) (in Europe) up to 5 h, although the difference between consecutive observations is low (Villaescusa-Nadal et al. 2019b). The drift effect changes in each satellite and it might not be constant at the time. Accordingly, SZA creates spurious trends, which can be false trends or lack of the real trends (Latifovic et al. 2012), according to the diurnal cycle amplitude of the geophysical properties (Devasthale et al. 2012; Tian et al. 2015). Those trends are identified as a systematic error and reveals significant differences between AVHRR-2 and AVHRR-3 (Latifovic et al. 2012), being greater during 1982–2000 (Tian et al. 2015). Also, depending on the several features: year season, location, latitude, atmosphere, region, land cover, vegetation types; the influence varies (Privette et al. 1995; Weber and Wunderle 2019) such as in semi-arid, arid and hyper-arid regions where it has more impact (Tian et al. 2015), morphology (Sellers et al. 1994), or lower latitudes, which presents the greatest errors (Stengel et al. 2020).

Some corrections have been applied in different studies to optimize the accuracy of the data or to improve their applications (Weber and Wunderle 2019), using the SZA channel. Gutman (1999) applied a simple formulation to correct temperatures and a simple least-square for the time series, dividing the global data in six vegetation classes. Lieberherr and Wunderle (2018) corrected temperatures with their own model. Latifovic et al. (2012) developed some two-phase correction. Devasthale et al. (2012) used a rotated empirical orthogonal function analysis (REOF). Privette et al. (1995) bore in mind in their equations the latitudes, and Sellers et al. (1994) the class cover. Other analyses remove pixels with high SZA (Los et al. 1994) or the years most affected (Ji and Brown 2017).

	Fire_cci ATBD AVHRR-LTDR	Ref.:	Fire_cci_D2.1.3_ATBD-AVHRR-LTDR_v1.0		
		Issue	1.0	Date	19/11/2021
		Page	25		

BA can be widely influenced by SZA since in Weber and Wunderle (2019) the number of observed fires decreases by 90%, which was also observed to be associated to the BA detection in the beta version of our product (Giglio and Roy 2020). In our case, we have created a relative parameter, to include in the Corrected Otsu threshold, in the most affected period (1982-2000) to correct this SZA effect. SZAc correction parameter was calculated with the $\overline{SZA}_{m,CR}$ (particular month (m) and continental region(CR)) divided between the mean of the Min ($SZA_{m,CR}$) in the period of the time series more affected (1982-2000), which was the corrected.

$$SZAc_{correction_{m,CR}} = \frac{\overline{SZA}_{m,CR}}{\text{Min}(SZA_{m,CR})} \quad (8)$$

A relative parameter was more accurate (Latifovic et al. 2012) used as a coefficients of an exponential function (Sellers et al. 1994), as seen in the SZA correction influences on the Relative constant to corrected Otsu in our study. Thereby, the pixels more SZA affected were smoother by the relative constant, and the correction did not affect to Otsu so much. It means, the signal affected by SZA decreased and might give lower probabilities, so reducing the relative constant to detect attenuated signals captured by Otsu.

$$\begin{aligned} \text{Corrected Threshold}_{Otsu,m,CR} \\ = \text{Threshold}_{Otsu,m,CR} * (\text{Relative constant}_{m,CR})^{SZAc_{correction_{m,CR}}} \end{aligned} \quad (9)$$

Due to the fact that large angles are the cause of the greatest changes (Stengel et al. 2020) and affecting some latitudes or regions more than others, we created a previous requirement, and include that correction per image, month and continental region (Privette et al. 1995). If the correlation between SZA and Otsu was less than 75%, the relation was not consider too high to correct and we trusted that previous threshold solved this relation; if r Pearson was between 75% and 90%, we applied the SZA correction; and when the correlation was more than 90%, the SZA correction was elevated to the second power because there was a very high SZA distortion.

If r Pearson (SZA-Otsu) < 75%:

$$\text{Corrected Threshold}_{Otsu,m,CR} = \text{Threshold}_{Otsu,m,CR} * \text{Relative constant}_{m,CR} \quad (9.1)$$


If r Pearson (SZA-Otsu) between 75-90%:

$$\begin{aligned} \text{Corrected Threshold}_{Otsu,m,CR} \\ = \text{Threshold}_{Otsu,m,CR} * (\text{Relative constant}_{m,CR})^{SZAc_{correction_{m,CR}}} \end{aligned} \quad (9.2)$$

If r Pearson (SZA-Otsu) > 90%:

$$\begin{aligned} \text{Corrected Threshold}_{Otsu,m,CR} \\ = \text{Threshold}_{Otsu,m,CR} * (\text{Relative constant}_{m,CR})^{(SZAc_{correction_{m,CR}})^2} \end{aligned} \quad (9.3)$$

Therefore, a sample with a high SZA has an attenuated signal in the daily data, monthly composite and LBI. Once RF was classified, lower probability was assigned to this sample than a similar sample without SZA influence. After Otsu gave a threshold, the sample object did not have so much separability and stayed closer to the cut-off threshold. When Otsu was corrected, we tried to fit it to the optimum DC, but the adjustment should be much slighter not to lose that sample.

	Fire_cci ATBD AVHRR-LTDR	Ref.:	Fire_cci_D2.1.3_ATBD-AVHRR-LTDR_v1.0		
		Issue	1.0	Date	19/11/2021
		Page	26		

After applying the corrected Otsu in each image per month and region in both model results (global and boreal), a binary classification was achieved where the thresholds have been adapted to each image and region and SZA has been corrected.

Despite those corrections, the lack of data and the decrease of good observations cannot be corrected and this must be taking into account as a limitation of the input data.

2.4.2 Proportions

In this step, BA proportions were developed to make a realistic classification where a pixel of 0.05° ($\approx 25\text{km}^2$) can be burned among 0.000 to 1.000%. A soft classification is more accurate than a hard classification; although a pixel may have commission and omission errors, it will be less affected by them (Pepe et al. 2010). In our case, a mixed coverage of a pixel of 0.05° between burned-unburned reduced especially the commission.

The objective was to achieve a relationship between FireCCI51 and the binary classification (obtained in the previous step) that provided a similar total BA for the overlapping period, and then spanned that relation to extrapolate backwards. Therefore, an analysis (Otón et al. 2019) was done at grid-cell level (0.25°) each month in the FireCCI51 period, so that the spatial aggregation influence and spatial coherence (vicinity) were developed (Lizundia-Loiola et al. 2020). FireCCI51 BA was calculated for each cell (0.25°) during the overlapping period. Afterwards, the proportion of burned pixels (binary classification) that would sum up the total BA of FireCCI51 was estimated for each cell (0.25°). Four different cases were found (A to D in Figure 10). Case A was when both FireCCI51 and the binary classification detected BA. In that case, the BA proportion was obtained by dividing the total BA detected by FireCCI51 during the target month by the total BA obtained in the binary RF classification (2001-2018). Where FireCCI51 detected BA but the binary classification did not (case B) in the common time series, the area of one pixel was considered as the total BA in the binary classification. Where cells were never detected as BA in the FireCCI51 period but the binary classification detected some (case C), or where FireCCI51 and the binary classification did not detect BA in that month during the 2001-2018 time series (case D), the median of the BA proportions (Case A and B) of each continental region was used. Median proportion is a novelty from the beta version and a similar concept was applied in GFED4 from GFED3 (Giglio et al. 2013). Thereby, median proportion in previously undetected pixels reduced the omission error. A limitation of this method was a possible border effect (analysed in Otón et al. (2021c)), but we deemed that the proportion and the error would be small. The last condition was that a pixel could not be fully burned in a temporal window of six consecutive months.

The final FireCCILT11 product was created substituting the global results in the boreal region with the results of the boreal model.

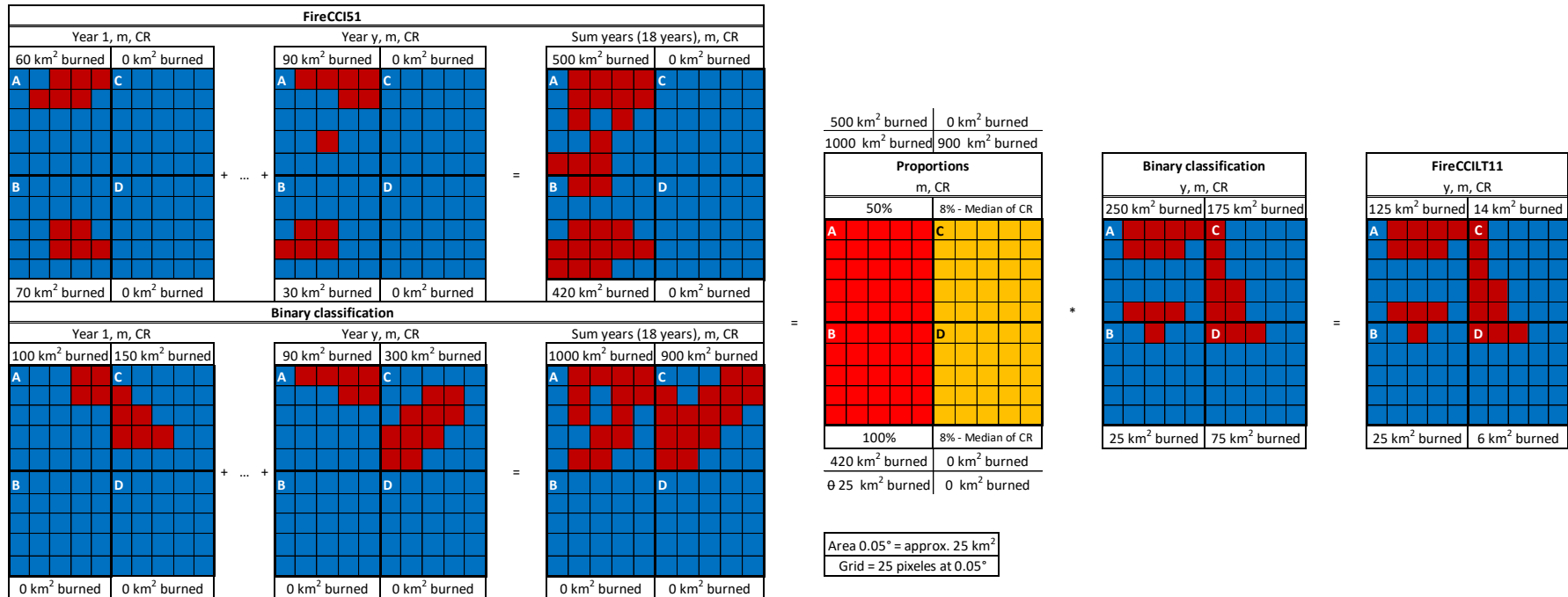


Figure 10. Calculation of BA proportions per grid cells (0.25°). This example shows the four classification possibilities (A-D), where y is the year, m is the month, and CR is each of the continental regions. The figure shows in the upper left the sum of FireCCI51 BA of the different years (2001-2018) and in the lower left the sum of the Binary classification BA (obtained from the RF algorithm, and deemed fully burned). In the centre, the BA proportions allocated to each grid cell is shown, which multiplied by the BA in each Binary classification image in the 1982-2018 time series allows to obtain the total burned area in each pixel.

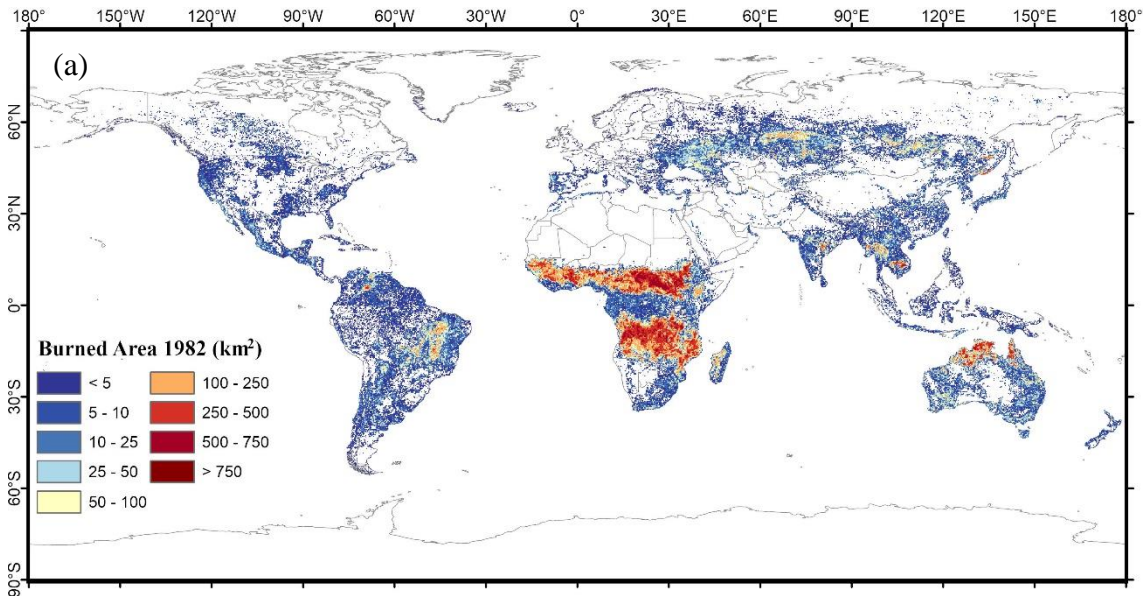


2.5 FireCCILT11 product

The algorithm was run with the available time series of LTDR data (1982-2018, except 1994) to create the FireCCILT11 dataset, comprised by two products: monthly pixel files at 0.05° resolution, including date of detection according to the composite, confidence level, burned area and number of observations, and monthly grid files at 0.25° resolution, including for each cell, total burned area, standard error, fraction of burnable area and proportion of observed area.

Figure 11 shows the spatial distribution of total BA for two years. The spatial patterns of BA are consistent with other global BA products, with higher occurrence in the Tropical dry belts, particularly in Africa, Northern Australia, Colombia-Venezuela and Brazil, Cambodia, Eastern India, and Central Asia (Otón et al. 2021b; Otón et al. 2021c). As in other global BA products, the FireCCILT11 product estimated that Africa was the most extensively burned continent (with 66% of global BA). Spatial trends were similar in the time series, including periods when the LTDR input was obtained from the AVHRR2 sensor (before 2000) and from the AVHRR3 (after 2000), as observed in the examples of figure 4. Temporal trends were analysed in Otón et al. (2021c).

The annual BA average estimated by the FireCCILT11 product was 4.59 Mkm², with an accumulated BA of 165.26 Mkm² for the period 1982-2018 (excluding 1994), of which 79.08 Mkm² were from 1982-2000 and 86.18 Mkm² from 2001-2018. The maximum annual BA was observed in 2011, with 5.18 Mkm², and the least-burned year was 1991 with 4.09 Mkm². August was the month with the largest BA, with an average of 0.63 Mkm², and March was the smallest with 0.15 Mkm².



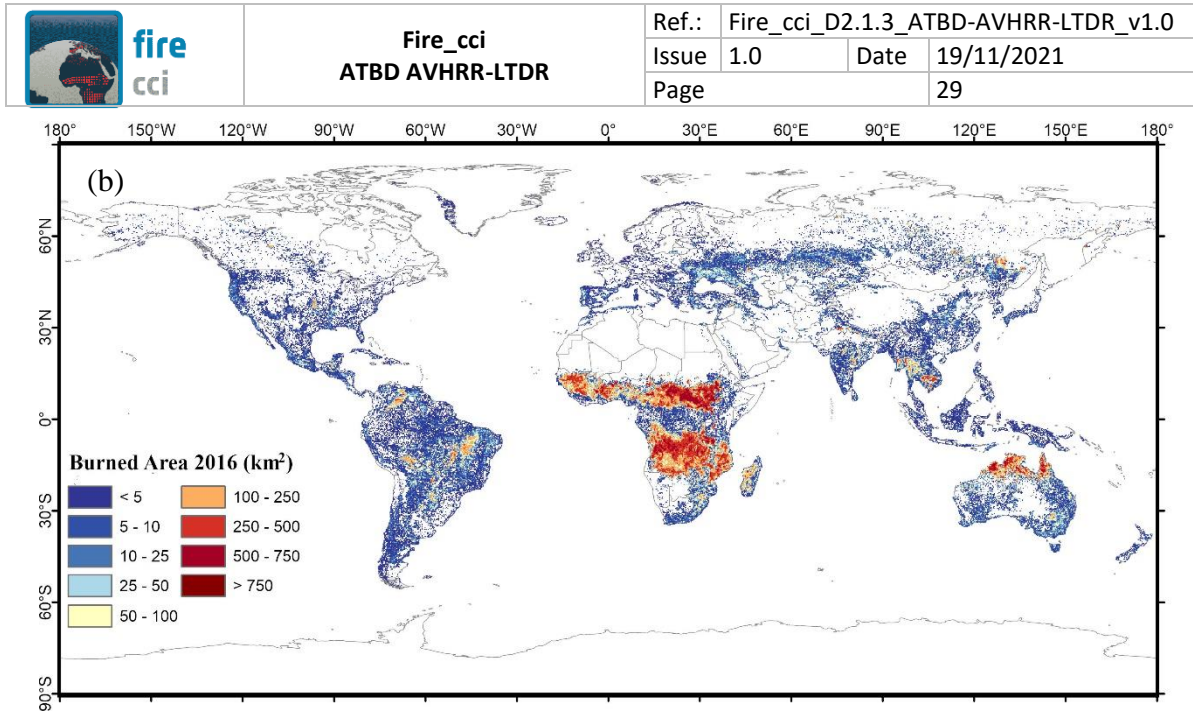


Figure 11. Annual FireCCI11 BA (at 0.25° resolution) for two different periods: (a) 1982 belongs to the 1982-2000 period with the AVHRR2 sensor, and (b) 2016 belongs to the 2001-2018 period with the AVHRR3 sensor.

2.5.1 Accuracy assessment

The inter-comparison (Annex 2: Inter-comparison) and validation (Annex 3: Validation) of the global long-term low resolution product is hard work but is absolutely needed to assess the accuracy of that product. On the one hand, spatial and temporal consistency of the product is checked with global BA products available (shorter times series), official perimeters (regional but long-term) and regional studies (literature) (Otón et al. 2021b). On the other hand, the creation of a Landsat dataset to validate the product, as has been proposed by different authors (Boschetti et al. 2006; Padilla et al. 2017; Padilla et al. 2015), using CEOS-LPVS protocols (<http://lpvs.gsfc.nasa.gov>, accessed October 2021) is unrealistic since the human effort would be too high and the procurement of images could be limited (Wulder et al. 2016). Thereby, a small but long-term Landsat dataset was created in the most fire affected region (Otón et al. 2021a).


Commission error (Ce), Omission error (Oe), real Bias (rB) and Dice Coefficient (DC) were calculated (Annex 2: Inter-comparison, Otón et al. 2021b, Annex 3: Validation, Otón et al. 2021a) because they are the most common statistical measures in current BA validations (Lizundia-Loiola et al. 2020; Padilla et al. 2017; Padilla et al. 2015; Roteta et al. 2019). Also, trends and r Pearson are designed to show the correlation and behavior of the product (Otón et al. 2021a, Otón et al. 2021b, Otón et al. 2021c).

$$Ce = \frac{\text{False Positives}}{\text{Total Burned of the Product Classification}} \quad (10)$$

$$Oe = \frac{\text{False Negatives}}{\text{Total Burned of the Reference Classification}} \quad (11)$$

$$\text{Dice Coefficient} = \frac{2 \cdot \text{True Positives}}{2 \cdot \text{True Positives} + \text{False Positives} + \text{False Negatives}} \quad (12)$$

$$\text{relB} = \frac{\text{False Positives} - \text{False Negatives}}{\text{Total Burned of the Reference Classification}} \quad (13)$$

	Fire_cci ATBD AVHRR-LTDR	Ref.: Fire_cci_D2.1.3_ATBD-AVHRR-LTDR_v1.0
		Issue 1.0 Date 19/11/2021
		Page 30

References

- Alcaraz-Segura, D., Chuvieco, E., Epstein, H.E., Kasischke, E.S., & Trishchenko, A. (2010). Debating the greening vs. browning of the North American boreal forest: differences between satellite datasets. *Global Change Biology*, *16*, 760-770
- Alonso-Canas, I., & Chuvieco, E. (2015). Global burned area mapping from ENVISAT-MERIS and MODIS active fire data. *Remote Sensing Of Environment*, *163*, 140-152
- Amos, C., Petropoulos, G.P., & Ferentinos, K.P. (2019). Determining the use of Sentinel-2A MSI for wildfire burning & severity detection. *International Journal of Remote Sensing*, *40*, 905-930
- Anaya, J.A., & Chuvieco, E. (2012). Accuracy Assessment of Burned Area Products in the Orinoco Basin. *Photogrammetric Engineering and Remote Sensing*, *78*, 53-60
- Barbosa, P.M., Grégoire, J.M., & Pereira, J.M.C. (1999). An algorithm for extracting burned areas from time series of AVHRR GAC data applied at a continental scale. *Remote Sensing Of Environment*, *69*, 253-263
- Bastarrika, A., Barrett, B., Roteta, E., Akizu, O., Mesanza, A., Torre, L., Anaya, J.A., Rodriguez-Montellano, A., & Chuvieco, E. (2018). Mapping burned areas in Latin America from Landsat-8 with Google Earth Engine. *Remote Sensing*
- Beck, H.E., McVicar, T.R., van Dijk, A.I., Schellekens, J., de Jeu, R.A., & Bruijnzeel, L.A. (2011). Global evaluation of four AVHRR-NDVI data sets: Intercomparison and assessment against Landsat imagery. *Remote Sensing Of Environment*, *115*, 2547-2563
- Bin, W., Ming, L., Dan, J., Suju, L., Qiang, C., Chao, W., Yang, Z., Huan, Y., & Jun, Z. (2019). A Method of Automatically Extracting Forest Fire Burned Areas Using Gf-1 Remote Sensing Images. In, *IGARSS 2019-2019 IEEE International Geoscience and Remote Sensing Symposium* (pp. 9953-9955): IEEE
- Boschetti, L., Brivio, P.A., Eva, H.D., Gallego, J., Baraldi, A., & Gregoire, J.M. (2006). A sampling method for the retrospective validation of Global Burned Area products. *IEEE Transactions On Geoscience and Remote Sensing*, *44*, 1765-1773
- Boschetti, L., Flasse, S.P., & Brivio, P.A. (2004). Analysis of the conflict between omission and commission in low spatial resolution dichotomic thematic products: The Pareto Boundary. *Remote Sensing Of Environment*, *91*, 280-292
- Breiman, L. (2001). Random forests. *Machine learning*, *45*, 5-32
- Brown, A.R., Petropoulos, G.P., & Ferentinos, K.P. (2018). Appraisal of the Sentinel-1 & 2 use in a large-scale wildfire assessment: A case study from Portugal's fires of 2017. *Applied Geography*, *100*, 78-89
- Bunn, A.G., & Goetz, S.J. (2006). Trends in satellite-observed circumpolar photosynthetic activity from 1982 to 2003: The influence of seasonality, cover type, and vegetation density. *Earth Interactions*, *10*, Paper n. 12: 11-19
- Canadian Forest Service (2017). Canadian National Fire Database – Agency Fire Data. *Natural Resources Canada, Canadian Forest Service, Northern Forestry Centre, Edmonton, Alberta*. Available online: <http://cwfis.cfs.nrcan.gc.ca/ha/nfdb>, last accessed on October 2021.
- Carmona-Moreno, C., Belward, A., Malingreau, J.P., Hartley, A., Garcia-Alegre, M., Antonovskiy, M., Buchshtaber, V., & Pivovarov, V. (2005). Characterizing interannual variations in global fire calendar using data from Earth observing satellites. *Global Change Biology*, *11*, 1537-1555
- Cihlar, J., Manak, D., & D'Iorio, M. (1994). Evaluation of compositing algorithms for AVHRR data over land. *IEEE Transactions On Geoscience and Remote Sensing*, *32*, 427-437

	Fire_cci ATBD AVHRR-LTDR	Ref.: Fire_cci_D2.1.3_ATBD-AVHRR-LTDR_v1.0
		Issue 1.0 Date 19/11/2021
		Page 31

- Copernicus (2019). Algorithm Theoretical Basis Document, ICDR Land Cover 2016. Copernicus Climate Change Service: Louvain, Belgium, 62p. Available online: <https://cds.climate.copernicus.eu/>, last accessed on October 2021.
- Cosnefroy, H., Leroy, M., & Briottet, X. (1996). Selection and characterization of Saharan and Arabian desert sites for the calibration of optical satellite sensors. *Remote Sensing Of Environment*, 58, 101-114
- Csiszar, I., Abuelgasim, A., Li, Z.Q., Jin, J.Z., Fraser, R., & Hao, W.M. (2003). Interannual changes of active fire detectability in North America from long-term records of the advanced very high resolution radiometer. *Journal Of Geophysical Research-Atmospheres*, 108, 4075, doi:4010.1029/2001JD001373,
- Chuvieco, E., Englefield, P., Trishchenko, A.P., & Luo, Y. (2008). Generation of long time series of burn area maps of the boreal forest from NOAA–AVHRR composite data. *Remote Sens. Environ.*, 112, 2381-2396
- Chuvieco, E., Lizundia-Loiola, J., Pettinari, M.L., Ramo, R., Padilla, M., Tansey, K., Mouillot, F., Laurent, P., Storm, T., & Heil, A. (2018). Generation and analysis of a new global burned area product based on MODIS 250 m reflectance bands and thermal anomalies. *Earth System Science Data*, 10, 2015-2031
- Chuvieco, E., Martín, M.P., & Palacios, A. (2002). Assessment of different spectral indices in the red-near-infrared spectral domain for burned land discrimination. *International Journal of Remote Sensing*, 23, 5103-5110
- Chuvieco, E., Ventura, G., Martín, M.P., & Gomez, I. (2005). Assessment of multitemporal compositing techniques of MODIS and AVHRR images for burned land mapping. *Remote Sensing Of Environment*, 94, 450 – 462
- Devasthale, A., Karlsson, K.-G., Quaas, J., & Graßl, H. (2012). Correcting orbital drift signal in the time series of AVHRR derived convective cloud fraction using rotated empirical orthogonal function. *Atmospheric Measurement Techniques*, 5, 267-273
- Dice, L.R. (1945). Measures of the amount of ecologic association between species. *Ecology*, 26, 297-302
- Dillon, G.K., Holden, Z.A., Morgan, P., Crimmins, M.A., Heyerdahl, E.K., & Luce, C.H. (2011). Both topography and climate affected forest and woodland burn severity in two regions of the western US, 1984 to 2006. *Ecosphere*, 2, 1-33
- Dubinin, M., Potapov, P., Lushchekina, A., & Radeloff, V.C. (2010). Reconstructing long time series of burned areas in arid grasslands of southern Russia by satellite remote sensing. *Remote Sensing Of Environment*, 114, 1638-1648
- Dwyer, E., Pereira, J.M.C., Grégorie, J.-M., & DaCamara, C.C. (2000). Characterization of the spatio-temporal patterns of global fire activity using satellite imagery for the period April 1992 to March 1993. *Journal of Biogeography*, 27, 57-69
- Eidenshink, J., Schwind, B., Brewer, K., Zhu, Z.-L., Quayle, B., & Howard, S. (2007). A project for monitoring trends in burn severity. *Fire Ecology*, 3, 3-21
- El Saleous, N., Vermote, E., Justice, C., Townshend, J., Tucker, C., & Goward, S. (2000). Improvements in the global biospheric record from the Advanced Very High Resolution Radiometer (AVHRR). *International Journal of Remote Sensing*, 21, 1251-1277
- Erdenesaikhan, N., & Erdenetuya, M. (1999). Forest and steppe fire monitoring in Mongolia using satellite remote sensing. *International Forest Fire News*, 21, 71-74
- ESA (2013). Land Cover CCI: Algorithm Theoretical Basis Document Version 2., ESA: Louvain, Belgium, 191p. Available online: https://climate.esa.int/media/documents/Land_Cover_CCI_ATBDv2_2.3.pdf, last accessed on October 2021.
- Eva, H., & Lambin, E.F. (1998). Remote Sensing of Biomass Burning in Tropical Regions: Sampling Issues and Multisensor Approach. *Remote Sensing Of Environment*, 64, 292-315

	Fire_cci ATBD AVHRR-LTDR	Ref.: Fire_cci_D2.1.3_ATBD-AVHRR-LTDR_v1.0
		Issue 1.0 Date 19/11/2021
		Page 32

- Fraser, R.H., Hall, R.J., Landry, R., Lynham, T., Raymond, D., Lee, B., & Li, Z. (2004). Validation and calibration of Canada-wide coarse-resolution satellite burned-area maps. *Photogrammetric Engineering and Remote Sensing*, 70, 451-460
- Fraser, R.H., Li, Z., & Cihlar, J. (2000). Hotspot and NDVI Differencing Synergy (HANDS): a new technique for burned area mapping over boreal forest. *Remote Sensing Of Environment*, 74, 362-376
- García-Lázaro, J., Moreno-Ruiz, J., Riaño, D., & Arbelo, M. (2018). Estimation of burned area in the Northeastern Siberian Boreal Forest from a long-term data record (LTDR) 1982–2015 time series. *Remote Sensing*, 10, 940
- Giglio, L. (2007). Characterization of the tropical diurnal fire cycle using VIRS and MODIS observations. *Remote Sensing Of Environment*, 108, 407-421
- Giglio, L., Boschetti, L., Roy, D.P., Humber, M.L., & Justice, C.O. (2018). The Collection 6 MODIS burned area mapping algorithm and product. *Remote Sensing Of Environment*, 217, 72-85
- Giglio, L., Randerson, J.T., van der Werf, G.R., Kasibhatla, P.S., Collatz, G.J., Morton, D.C., & DeFries, R.S. (2010). Assessing variability and long-term trends in burned area by merging multiple satellite fire products. *Biogeosciences Discuss.*, 7, 1171-1186, doi:1110.5194/bg-1177-1171-2010,
- Giglio, L., Randerson, J.T., & Werf, G.R. (2013). Analysis of daily, monthly, and annual burned area using the fourth generation global fire emissions database (GFED4). *Journal of Geophysical Research: Biogeosciences*, 118, 317-328
- Giglio, L., & Roy, D. (2020). On the outstanding need for a long-term, multi-decadal, validated and quality assessed record of global burned area: Caution in the use of Advanced Very High Resolution Radiometer data. *Science of Remote Sensing*, 2, 100007
- Granier, C., Bessagnet, B., Bond, T., D'Angiola, A., van Der Gon, H.D., Frost, G.J., Heil, A., Kaiser, J.W., Kinne, S., & Klimont, Z. (2011). Evolution of anthropogenic and biomass burning emissions of air pollutants at global and regional scales during the 1980–2010 period. *Climatic Change*, 109, 163-190
- Grégoire, J.M., Tansey, K., & Silva, J.M.N. (2003). The GBA2000 initiative: Developing a global burned area database from SPOT-VEGETATION imagery. *International Journal of Remote Sensing*, 24, 1369 - 1376
- Gutman, G. (1999). On the monitoring of land surface temperatures with the NOAA/AVHRR: removing the effect of satellite orbit drift. *International Journal of Remote Sensing*, 20, 3407-3413
- Hansen, M., Song, X., DiMiceli, C., Carroll, M., Sohlberg, R., Kim, D.-H., & Townshend, J. (2018). MEaSURES Vegetation Continuous Fields ESDR: Algorithm Theoretical Basis Document (ATBD), Version 2.0. Available online: https://lpdaac.usgs.gov/documents/144/VCF5KYR_ATBD.pdf, last accessed on October 2021.
- Hantson, S., Arneth, A., Harrison, S.P., Kelley, D.I., Prentice, I.C., Rabin, S.S., Archibald, S., Mouillot, F., Arnold, S.R., & Artaxo, P. (2016). The status and challenge of global fire modelling. *Biogeosciences*, 13, 3359-3375
- Huang, L., Fang, Y., Zuo, X., & Yu, X. (2015). Automatic change detection method of multitemporal remote sensing images based on 2D-otsu algorithm improved by firefly algorithm. *Journal of Sensors*, 2015
- Ignatov, A., Laszlo, I., Harrod, E., Kidwell, K., & Goodrum, G. (2004). Equator crossing times for NOAA, ERS and EOS sun-synchronous satellites. *International Journal of Remote Sensing*, 25, 5255-5266

	Fire_cci ATBD AVHRR-LTDR		Ref.:	Fire_cci_D2.1.3_ATBD-AVHRR-LTDR_v1.0		
			Issue	1.0	Date	19/11/2021
			Page	33		

- Jain, P., Coogan, S.C., Subramanian, S.G., Crowley, M., Taylor, S., & Flannigan, M.D. (2020). A review of machine learning applications in wildfire science and management. *arXiv preprint arXiv:2003.00646*
- James, M., & Kalluri, S.N. (1994). The Pathfinder AVHRR land data set: an improved coarse resolution data set for terrestrial monitoring. *International Journal of Remote Sensing*, *15*, 3347-3363
- Ji, L., & Brown, J.F. (2017). Effect of NOAA satellite orbital drift on AVHRR-derived phenological metrics. *International Journal of Applied Earth Observation and Geoinformation*, *62*, 215-223
- Justice, C., Belward, A., Morisette, J., Lewis, P., Privette, J., & Baret, F. (2000). Developments in the validation of satellite sensor products for the study of the land surface. *International Journal of Remote Sensing*, *21*, 3383-3390
- Justice, C., Markham, B., Townshend, J., & Kennard, R. (1989). Spatial degradation of satellite data. *International Journal of Remote Sensing*, *10*, 1539-1561
- Katagis, T., Gitas, I.Z., Toukiloglou, P., Veraverbeke, S., & Goossens, R. (2014). Trend analysis of medium-and coarse-resolution time series image data for burned area mapping in a Mediterranean ecosystem. *International Journal of Wildland Fire*, *23*, 668-677
- Kaufmann, R.K., Zhou, L., Knyazikhin, Y., Shabanov, V., Myneni, R.B., & Tucker, C.J. (2000). Effect of orbital drift and sensor changes on the time series of AVHRR vegetation index data. *IEEE Transactions On Geoscience and Remote Sensing*, *38*, 2584-2597
- Kittler, J., & Illingworth, J. (1985). On threshold selection using clustering criteria. *IEEE transactions on systems, man, and cybernetics*, 652-655
- Kucêra, J., Yasuoka, Y., & Dye, D.G. (2005). Creating a forest fire database for the Far East of Asia using NOAA/AVHRR observation. *International Journal of Remote Sensing*, *26*, 2423-2439
- Kumar, A., & Tiwari, A. (2019). A Comparative Study of Otsu Thresholding and K-means Algorithm of Image Segmentation. *International Journal of Engineering and Technical Research (IJETR)*. Volume-9, Issue-5, 2454-4698 . ISSN: 2321-0869.
- Latifovic, R., Pouliot, D., & Dillabaugh, C. (2012). Identification and correction of systematic error in NOAA AVHRR long-term satellite data record. *Remote Sensing Of Environment*, *127*, 84-97
- Li, Z., Kaufman, Y.J., Ichoku, C., Fraser, R., Trishchenko, A., Giglio, L., Jin, J., & Yu, X. (2001). A review of AVHRR-based active fire detection algorithms: Principles, limitations, and recommendations. *Global and regional vegetation fire monitoring from space, planning and coordinated international effort*, 199-225
- Lieberherr, G., & Wunderle, S. (2018). Lake surface water temperature derived from 35 years of AVHRR sensor data for European lakes. *Remote Sensing*, *10*, 990
- Lizundia-Loiola, J., Otón, G., Ramo, R., & Chuvieco, E. (2020). A spatio-temporal active-fire clustering approach for global burned area mapping at 250 m from MODIS data. *Remote Sensing Of Environment*, *236*, 111493
- Long, T., Zhang, Z., He, G., Jiao, W., Tang, C., Wu, B., Zhang, X., Wang, G., & Yin, R. (2018). 30m resolution Global Annual Burned Area Mapping based on Landsat images and Google Earth Engine. *arXiv preprint arXiv:1805.02579*
- Los, S.O., Justice, C., & Tucker, C. (1994). A global 1 by 1 NDVI data set for climate studies derived from the GIMMS continental NDVI data. *International Journal of Remote Sensing*, *15*, 3493-3518
- McGregor, J., & Gorman, A.J. (1994). Some considerations for using AVHRR data in climatological studies: orbital characteristics of NOAA satellites. *International Journal of Remote Sensing*, *15*, 537-548

	fire cci	Fire_cci ATBD AVHRR-LTDR		Ref.: Fire_cci_D2.1.3_ATBD-AVHRR-LTDR_v1.0	
		Issue	1.0	Date	19/11/2021
		Page	34		

- Melchiorre, A., & Boschetti, L. (2018). Global analysis of burned area persistence time with MODIS data. *Remote Sensing*, *10*, 750
- Moreno-Ruiz, J.A., García-Lázaro, J.R., Arbelo, M., & Cantón-Garbín, M. (2020). MODIS Sensor Capability to Burned Area Mapping—Assessment of Performance and Improvements Provided by the Latest Standard Products in Boreal Regions. *Sensors*, *20*, 5423
- Moreno-Ruiz, J.A., García-Lázaro, J.R., Arbelo, M., & Riaño, D. (2019). A Comparison of Burned Area Time Series in the Alaskan Boreal Forests from Different Remote Sensing Products. *Forests*, *10*, 363
- Moreno-Ruiz, J.A., García-Lázaro, J.R., Riaño, D., & Kefauver, S.C. (2013). The Synergy of the 0.05° (5km) AVHRR Long-Term Data Record (LTDR) and Landsat TM Archive to Map Large Fires in the North American Boreal Region From 1984 to 1998. *IEEE Journal of Selected Topics in Applied Earth Observations and Remote Sensing*, *7*, 1157-1166
- Moreno-Ruiz, J.A., Riano, D., Arbelo, M., French, N.H., Ustin, S.L., & Whiting, M.L. (2012). Burned area mapping time series in Canada (1984–1999) from NOAA-AVHRR LTDR: A comparison with other remote sensing products and fire perimeters. *Remote Sensing Of Environment*, *117*, 407-414
- Mouillot, F., & Field, C.B. (2005). Fire history and the global carbon budget: a 1 degrees x 1 degrees fire history reconstruction for the 20th century. *Global Change Biology*, *11*, 398-420
- Mouillot, F., Schultz, M.G., Yue, C., Cadule, P., Tansey, K., Ciais, P., & Chuvieco, E. (2014). Ten years of global burned area products from spaceborne remote sensing—A review: Analysis of user needs and recommendations for future developments. *International Journal of Applied Earth Observation and Geoinformation*, *26*, 64-79
- Oliva, P., Martin, P., & Chuvieco, E. (2011). Burned area mapping with MERIS post-fire image. *International Journal of Remote Sensing*, *32*, 4175-4201
- Otón, G., & Chuvieco, E. (2018). ESA CCI ECV Fire Disturbance: O2.D2 Algorithm Theoretical Basis Document (ATBD) for AVHRR LTDR data, version 1.1. Available online: <https://climate.esa.int/en/projects/fire/key-documents/>, last accessed on October 2021.
- Otón, G., Franquesa, M., Lizundia-Loiola, J., & Chuvieco, E. (2021a). Validation of low spatial resolution and no-dichotomy global long-term burned area product by Pareto boundary. In, *Earth Resources and Environmental Remote Sensing/GIS Applications XII* (pp. 293-299): SPIE
- Otón, G., Lizundia-Loiola, J., Pettinari, L., & Chuvieco, E. (2021b). Development of a Consistent Global Long-Term Burned Area product (1982-2018) based on AVHRR-LTDR data. *International Journal of Applied Earth Observation and Geoinformation*, *103*, 102473
- Otón, G., Pereira, J.M.C., Silva, J., & Chuvieco, E. (2021c). Analysis of Trends in the FireCCI Global Long Term Burned Area Product (1982–2018). *Fire*, *4*, 74
- Otón, G., Ramo, R., Lizundia-Loiola, J., & Chuvieco, E. (2019). Global Detection of Long-Term (1982–2017) Burned Area with AVHRR-LTDR Data. *Remote Sensing*, *11*, 2079
- Otón, G., Ramo, R., Lizundia-Loiola, J., & Chuvieco, E. (2020). Correction: Otón, G., et al. Global Detection of Long-Term (1982–2017) Burned Area with AVHRR-LTDR Data. *Remote Sensing* 2019, *11*, 2079. *Remote Sensing*, *12*, 2324
- Otsu, N. (1979). A threshold selection method from gray-level histograms. *IEEE transactions on systems, man, and cybernetics*, *9*, 62-66



- Padilla, M., Olofsson, P., Stehman, S.V., Tansey, K., & Chuvieco, E. (2017). Stratification and sample allocation for reference burned area data. *Remote Sensing Of Environment*, 203, 240-255
- Padilla, M., Stehman, S.V., Hantson, S., Oliva, P., Alonso-Canas, I., Bradley, A., Tansey, K., Mota, B., Pereira, J.M., & Chuvieco, E. (2015). Comparing the accuracies of remote sensing global burned area products using stratified random sampling and estimation. *Remote Sens. Environ.*, 160, 114-121
- Padilla, M., Wheeler, J., & Tansey, K. (2018). ESA CCI ECV Fire Disturbance: D4.1.1 Product Validation Report, version 2.1. Available online: <https://climate.esa.int/en/projects/fire/key-documents/>, last accessed on October 2020.
- Pedely, J., Devadiga, S., Masuoka, E., Brown, M., Pinzon, J., Tucker, C., Vermote, E., Prince, S., Nagol, J., Justice, C., Roy, D., Ju, J., Schaaf, C., Liu, J., Privette, J., & Pinheiro, A. (2007). Generating a long-term land data record from the AVHRR and MODIS instruments. In, *Geoscience and Remote Sensing Symposium, 2007. IGARSS 2007. IEEE International* (pp. 1021-1025): IEEE
- Pedregosa, F., Varoquaux, G., Gramfort, A., Michel, V., Thirion, B., Grisel, O., Blondel, M., Prettenhofer, P., Weiss, R., & Dubourg, V. (2011). Scikit-learn: Machine learning in Python. *the Journal of machine Learning research*, 12, 2825-2830
- Pepe, M., Boschetti, L., Brivio, P.A., & Rampini, A. (2010). Comparing the performance of fuzzy and crisp classifiers on remotely sensed images: A case of snow classification. *International Journal of Remote Sensing*, 31, 6189-6203
- Pinty, B., & Verstraete, M.M. (1992). GEMI: a non-linear index to monitor global vegetation from satellites. *Vegetatio*, 101, 15-20. <https://doi.org/10.1007/bf00031911>.
- Plank, S., Fuchs, E.-M., & Frey, C. (2017). A fully automatic instantaneous fire hotspot detection processor based on AVHRR Imagery—A TIMELINE thematic processor. *Remote Sensing*, 9, 30
- Plank, S., & Martinis, S. (2018). A Fully Automatic Burnt Area Mapping Processor Based on AVHRR Imagery—A TIMELINE Thematic Processor. *Remote Sensing*, 10, 341
- Power, M.J., Marlon, J.R., Bartlein, P.J., & Harrison, S.P. (2010). Fire history and the Global Charcoal Database: A new tool for hypothesis testing and data exploration. *Palaeogeography, Palaeoclimatology, Palaeoecology*, 291, 52-59
- Price, J.C. (1991). Timing of NOAA afternoon passes. *International Journal of Remote Sensing*, 12, 193-198
- Privette, J.L., Fowler, C., Wick, G.A., Baldwin, D., & Emery, W.J. (1995). Effects of orbital drift on Advanced Very High Resolution Radiometer products: Normalized Difference Vegetation Index and Sea Surface Temperature. *Remote Sensing Of Environment*, 53, 164-171
- Pu, R., Li, Z., Gong, P., Csiszar, I., Fraser, R., Hao, W., Kondragunta, S., Loboda, T., Hall, J., & Shevade, V. (2018). ABoVE: AVHRR-Derived Forest Fire Burned Area-Hot Spots, Alaska and Canada, 1989-2000. *ORNL DAAC*
- Qu, Z., & Zhang, L. (2010). Research on image segmentation based on the improved Otsu algorithm. In, *2010 Second International Conference on Intelligent Human-Machine Systems and Cybernetics* (pp. 228-231): IEEE
- Ramo, R., & Chuvieco, E. (2017). Developing a Random Forest Algorithm for MODIS Global Burned Area Classification. *Remote Sensing*, 9, 1193
- Ramo, R., García, M., Rodríguez, D., & Chuvieco, E. (2018). A data mining approach for global burned area mapping. *International Journal of Applied Earth Observation and Geoinformation*, 73, 39-51
- Ramo, R., Roteta, E., Bistinas, I., Van Wees, D., Bastarrika, A., Chuvieco, E., & Van der Werf, G.R. (2021). African burned area and fire carbon emissions are strongly impacted

	Fire_cci ATBD AVHRR-LTDR	Ref.: Fire_cci_D2.1.3_ATBD-AVHRR-LTDR_v1.0
		Issue 1.0 Date 19/11/2021
		Page 36

- by small fires undetected by coarse resolution satellite data. *Proceedings of the National Academy of Sciences*, 118, 1-7
- Riaño, D., Ruiz, J.M., Martínez, J.B., & Ustin, S. (2007). Burned area forecasting using past burned area records and Southern Oscillation Index for tropical Africa (1981–1999). *Remote Sensing Of Environment*, 107, 571-581
- Rodriguez-Galiano, V., Sanchez-Castillo, M., Chica-Olmo, M., & Chica-Rivas, M. (2015). Machine learning predictive models for mineral prospectivity: An evaluation of neural networks, random forest, regression trees and support vector machines. *Ore Geology Reviews*, 71, 804-818
- Rodriguez-Galiano, V.F., & Chica-Rivas, M. (2012). Evaluation of different machine learning methods for land cover mapping of a Mediterranean area using multi-seasonal Landsat images and Digital Terrain Models. *International Journal of Digital Earth*, 7, 492-509
- Rodriguez-Galiano, V.F., Ghimire, B., Rogan, J., Chica-Olmo, M., & Rigol-Sanchez, J.P. (2012). An assessment of the effectiveness of a random forest classifier for land-cover classification. *ISPRS Journal of Photogrammetry and Remote Sensing*, 67, 93-104
- Roteta, E., Bastarrika, A., Padilla, M., Storm, T., & Chuvieco, E. (2019). Development of a Sentinel-2 burned area algorithm: Generation of a small fire database for sub-Saharan Africa. *Remote Sensing Of Environment*, 222, 1-17
- Roy, D. (1997). Investigation of the maximum normalized difference vegetation index (NDVI) and the maximum surface temperature (Ts) AVHRR compositing procedures for the extraction of NDVI and Ts over forest. *International Journal of Remote Sensing*, 18, 2383-2401
- Roy, D., Frost, P., Justice, C., Landmann, T., Roux, J., Gumbo, K., Makungwa, S., Dunham, K., Du Toit, R., Mhwandagara, K., Zacarias, A., Tacheba, B., Dube, O., Pereira, J., Mushove, P., Morisette, J., Santhana, S., & Davies, D. (2005). The Southern Africa Fire Network (SAFNet) regional burned area product validation protocol. *International Journal of Remote Sensing*, 26, 4265-4292
- Roy, D.P., & Boschetti, L. (2009). Southern Africa Validation of the MODIS, L3JRC and GlobCarbon Burned-Area Products. *IEEE Transactions On Geoscience and Remote Sensing*, 47, DOI 10.1109/TGRS.2008.2009000
- Sellers, P.J., Tucker, C.J., Collatz, G.J., Los, S., Justice, C., Dazlich, D., & Randall, D. (1994). A global 1 by 1 NDVI data set for climate studies. Part 2: The generation of global fields of terrestrial biophysical parameters from the NDVI. *International Journal of Remote Sensing*, 15, 3519-3545
- Simon, M., Plummer, S., Fierens, F., Hoelzemann, J.J., & Arino, O. (2004). Burnt area detection at global scale using ATSR-2: The GLOBSCAR products and their qualification. *Journal of Geophysical Research - Atmospheres*, 109, D14S02, doi:10.1029/2002JD003622
- Stengel, M., Stapelberg, S., Sus, O., Finkensieper, S., Würzler, B., Philipp, D., Hollmann, R., Poulsen, C., Christensen, M., & McGarragh, G. (2020). Cloud_cci Advanced Very High Resolution Radiometer post meridiem (AVHRR-PM) dataset version 3: 35-year climatology of global cloud and radiation properties. *Earth System Science Data*, 12, 41-60
- Stroppiana, D., Pinnock, S., Pereira, J.M.C., & Grégorie, J.M. (2002). Radiometric analysis of SPOT-VEGETATION images for burnt area detection in Northern Australia. *Remote Sensing Of Environment*, 82, 21-37
- Thonicke, K., Venevsky, S., Sitch, S., & Cramer, W. (2001). The role of fire disturbance for global vegetation dynamics: coupling fire into a Dynamic Global Vegetation Model. *Global Ecology and Biogeography*, 10, 661-677

	Fire_cci ATBD AVHRR-LTDR	Ref.: Fire_cci_D2.1.3_ATBD-AVHRR-LTDR_v1.0
		Issue 1.0 Date 19/11/2021
		Page 37

- Tian, F., Fensholt, R., Verbesselt, J., Grogan, K., Horion, S., & Wang, Y. (2015). Evaluating temporal consistency of long-term global NDVI datasets for trend analysis. *Remote Sensing Of Environment*, *163*, 326-340
- Trishchenko, A.P., Fedosejevs, G., Li, Z., & Cihlar, J. (2002). Trends and uncertainties in thermal calibration of AVHRR radiometers onboard NOAA-9 to NOAA-16. *Journal of Geophysical Research: Atmospheres*, *107*, ACL 17-11-ACL 17-13
- Tucker, C.J., Pinzon, J.E., Brown, M.E., Slayback, D.A., Pak, E.W., Mahoney, R., Vermote, E.F., & El Saleous, N. (2005). An extended AVHRR 8-km NDVI dataset compatible with MODIS and SPOT vegetation NDVI data. *International Journal of Remote Sensing*, *26*, 4485-4498
- Unajan, M.C., Gerardo, B.D., & Medina, R.P. (2019). A modified otsu-based image segmentation algorithm (obisa). In, *Proceedings of the international multiconference of engineers and computer scientists* (pp. 363-366)
- Vala, H.J., & Baxi, A. (2013). A review on Otsu image segmentation algorithm. *International Journal of Advanced Research in Computer Engineering & Technology (IJARCET)*, *2*, 387-389
- Vermote, E., Justice, C., Csizsar, I., Eidenshink, J., Myneni, R., Baret, F., Masuoka, E., Wolfe, R., & Devadiga, S. (2009). A Terrestrial Surface Climate Data Record for Global Change Studies [PowerPoint slides]. Retrieved from <https://ltdr.modaps.eosdis.nasa.gov/ltdr/docs/AGU-Fall2009-vermote.pdf>.
- Vhengani, L., Frost, P., Lai, C., Booii, N., van den Dool, R., & Raath, W. (2015). Multitemporal burnt area mapping using Landsat 8: Merging multiple burnt area indices to highlight burnt areas. In, *2015 IEEE International Geoscience and Remote Sensing Symposium (IGARSS)* (pp. 4153-4156): IEEE
- Vijay, P.P., & Patil, N. (2016). Gray Scale Image Segmentation using OTSU Thresholding Optimal Approach. *Journal for Research*, *2*
- Villaescusa-Nadal, J.L., Franch, B., Roger, J.-C., Vermote, E.F., Skakun, S., & Justice, C. (2019a). Spectral adjustment model's analysis and application to remote sensing data. *IEEE Journal of Selected Topics in Applied Earth Observations and Remote Sensing*, *12*, 961-972
- Villaescusa-Nadal, J.L., Franch, B., Vermote, E.F., & Roger, J.-C. (2019b). Improving the AVHRR long term data record BRDF correction. *Remote Sensing*, *11*, 502
- Weber, H., & Wunderle, S. (2019). Drifting Effects of NOAA Satellites on Long-Term Active Fire Records of Europe. *Remote Sensing*, *11*, 467
- Wulder, M.A., White, J.C., Loveland, T.R., Woodcock, C.E., Belward, A.S., Cohen, W.B., Fosnight, E.A., Shaw, J., Masek, J.G., & Roy, D.P. (2016). The global Landsat archive: Status, consolidation, and direction. *Remote Sensing Of Environment*, *185*, 271-283
- Yates, C.P., Edwards, A.C., & Russell-Smith, J. (2009). Big fires and their ecological impacts in Australian savannas: size and frequency matters. *International Journal of Wildland Fire*, *17*, 768-781
- Zhan, Y., & Zhang, G. (2019). An improved OTSU algorithm using histogram accumulation moment for ore segmentation. *Symmetry*, *11*, 431
- Zhang, X., Tan, B., & Yu, Y. (2014). Interannual variations and trends in global land surface phenology derived from enhanced vegetation index during 1982–2010. *International Journal of Biometeorology*, *58*, 547-564

Annex 1: Acronyms and abbreviations

°C	Degree Celsius
ATBD	Algorithm Theoretical Basis Document
ATSR	Along Track Scanning Radiometers
AVHRR	Advanced Very High Resolution Radiometer
BA	Burned Area
BAI	Burned Area Index
BRDF	Bidirectional reflectance distribution function
BT	Brightness temperature
C3S	Copernicus Climate Change Service
CCI	Climate Change Initiative
CH	Channel
DC	Dice Coefficient
ECV	Essential Climate Variables
EPSG	European Petroleum Survey Group
ESA	European Space Agency
FireCCI51	MODIS Fire_cci burned area product, version 5.1
FireCCILT10	LTDR Fire_cci burned area product, version 1.0
FireCCILT11	LTDR Fire_cci burned area product, version 1.1
FOV	Field of View
GAC	Global Area Coverage
GCOS	Global Climate Observing System
GCS	Geographic Coordinate System
GEMI	Global Environmental Monitoring Index
GFED	Global Fire Emissions Database
GIMMS	Global Inventory Monitoring and Modeling System
HRPT	High-Resolution Picture Transmission

K	Kelvin
km	Kilometre
LAC	Local Area Coverage
LBI	LTDR Burned Index
LC	Land Cover
LTDR	Long Term Data Record
MaxT	Maximum temperature technique
MCD64A1	MODIS Burned Area product
MERIS	Medium Resolution Imaging Spectrometer
MODIS	Moderate Resolution Imaging Spectroradiometer
NASA	National Aeronautics and Space Administration
NBA	Unburned
NDVI	Normalized Difference Vegetation Index
NIR	Near-infrared
NN	Neural Network
NOAA	National Oceanic and Atmosphere Administration
QA	Quality assessment field
RELAZ	Relative azimuth
REOF	Rotated empirical orthogonal function analysis
RF	Random Forest
SREFL	Surface Reflectance
SVM	Super Vector Machine
SZEN	Solar zenith angle
SZA	Solar zenith angle
TOA	Top of Atmosphere
T5	Temperature Channel 5
VZEN	View zenith angle
σ	Standard deviations
μ	Mean
μm	Micrometre

	Fire_cci ATBD AVHRR-LTDR	Ref.:	Fire_cci_D2.1.3_ATBD-AVHRR-LTDR_v1.0			
		Issue	1.0	Date	19/11/2021	
		Page				39

Annex 2: Inter-comparison

1 BA databases

1.1 Global BA products

Currently, there are two global BA products used to compare the new BA product. FireCCI51 is the most accurate (Lizundia-Loiola et al. 2020) but it has been used to train FireCCILT11 (Otón et al. 2021b), and for this reason it could show some bias. The other well-known global BA product is MCD64A1 (Giglio et al. 2018), which also has an acceptable accuracy (Padilla et al. 2015). MCD64A1 is a global and monthly dataset at 250m, developed by NASA and generated from MODIS images from 2001 to date. We compared the global BA (trends and correlation) to FireCCILT10 beta (Otón et al. 2019), FireCCILT11, FireCCI51 and MCD64A1. Moreover, a continental regions analysis was done calculating the BA, and comparing with FireCCI51 and MCD64A1. In addition, a monthly study was performed to learn the behaviour of FireCCILT11 months with FireCCI51 and MCD64A1, and the monthly behaviour in previous years.

Furthermore, a SZA analysis was developed to test its correction, with SZA not affecting FireCCILT11. A global and regional analysis was done to show the correlation (r Pearson) among the beta version, new version and the number of good observations with the SZA.

1.2 Regional databases

1.2.1 Official perimeters and regional products

Afterward, long-term comparison is only available using the national official perimeters and MTBS although the latter has less accuracy before 2000 (pre-MODIS era) (Moreno-Ruiz et al. 2019). These data represent different regions and biomes, which were useful for learning the accuracy of FireCCILT11 in different parts of the world. The national official perimeters are not a ground truth and can contain errors (Canadian Forest Service 2017) but they are accurate data.

Tropical regions are compared in Australia from 2000 to 2018 using the North Australia and rangelands fire information (NAFI, Available online: <https://firenorth.org.au/nafi3/>, last accessed on October 2021) which generates BA through satellite data.

Boreal regions are compared in Canada and Alaska (USA). Canada, using the Canadian National Fire Database (CNFDB, Canadian Forest Service 2017) gives BA perimeters larger than 200 ha from 1980 to 2019. Alaska provides the Alaska fire history perimeters (AICC, Available online: <https://fire.ak.blm.gov/predsvcs/maps.php>, last accessed on October 2021) from 1940 to 2020. Alaska, as the years go by, provides more accurate data. This means that before 1987, only perimeters greater than 400 ha were provided, between 1987-1990, those greater than 40 ha were included, and after 1990 those greater than 4 ha.

Temperate regions are represented by USA, which has various state official perimeters, such as California (FRAP, Available online: <https://frap.fire.ca.gov/>, last accessed on October 2021), and Washington (Available online: <https://geo.wa.gov/>, last accessed on October 2021), but not a consistent national database although an approximation is found in Wildland Fire Decision Support System (WFDSS, Available online: https://wfdss.usgs.gov/wfdss_help/WFDSS_Help_Historical_Fire_Data.html, last accessed on October 2021). WFDSS is not a national official perimeters database. An

	Fire_cci ATBD AVHRR-LTDR		Ref.: Fire_cci_D2.1.3_ATBD-AVHRR-LTDR_v1.0	
			Issue 1.0	Date 19/11/2021
			Page 40	

integration of guidelines agreement, time series and features among them is necessary in order carry out a consistent analysis. The same thing happens in Europe (EFFIS, Available online: <https://effis.jrc.ec.europa.eu/>, last accessed on October 2021) where the inconsistency among countries does not allow a regional study. Thereby, MTBS (Eidenshink et al. 2007) is preferred for use because it has more consistency, although less accuracy before 2000. MTBS is created to study BA severity but contains large and historical BA perimeters. That database, from 1984 to 2017, is developed by historical perimeters (fire history database compilation, 1984-2003) and Landsat, and provides information on fires of more than 202 ha in the east and more than 404 ha in the west.

1.2.2 Regional BA studies

Also, we compared our product with other studies whose data extend back previous to 2000, and to places to which there was no other assess FireCCILT11. Several requirements were taken into account in order to do a consistent analysis:

1. There must be enough time series to study trends over ten years;
2. Some years had to be inside of MODIS years to assess its trends with MODIS product and check its coherence and consistency;
3. Analysis was done in places where there were no other reliable data such as BA products with more time series, larger study area or official perimeters;
4. Data available.

Studies like Barbosa et al. 1999 in Africa (1985/1986, 1986/1987, and 1990/1991), and Erdenesaikhan and Erdenetuya (1999) in Mongolia (1996-1998), are discarded because they had a limited time series of three years, Yates et al. (2009) had a time series of less than ten years (1997-2005) and we had data in Australia, or Kucêra et al. (2005) because it (1984-2001) did not have representation beyond the MODIS era. However, Dubinin et al. (2010), developed with AVHRR data, was selected to compare because it covered an area of 19.000 km² in the arid grasslands of southern Russia, and it extended twenty three years from 1985 to 2007. And the García-Lázaro et al. (2018) analysis, where BA estimation was performed in the Siberian Boreal Forest based on LTDR (v3, AVHRR and MODIS integrated), had also been used.

2 Results

2.1 Comparison with global BA products

The annual global patterns of FireCCILT11 BA are compared in Figure 12 with other BA products (precursor product and existing MODIS-based BA datasets). The trends of FireCCI51, MCD64A1 and FireCCILT11 are similar in the common time series, being high correlation (r Pearson) values (Table 4). MCD64A1-FireCCILT11 shows higher correlation (0.87) than FireCCI51-FireCCILT11 (0.60). Monthly values showed higher correlations, with r values of 0.89 (MCD64A1) and 0.95 (FireCCI51). FireCCILT11 presents higher monthly correlation with FireCCI51 since they show more similar trends when analysing the data on a monthly basis (Figure 13). This is because FireCCILT11 has been trained monthly with FireCCI51. But the yearly data (Figure 12) in FireCCILT11 is more similar to MCD64A1. The DC in the common time series of FireCCI51-FireCCILT11 is more than 0.63 ($O_e=0.21$ and $C_e=0.47$) and the DC of MCD64A1-FireCCILT11 is 0.44 ($O_e=0.39$ and $C_e=0.66$). Regarding BA, FireCCILT11 detects $\approx 3.5\%$ more than FireCCI51 and $\approx 14\%$ more than MCD64A1 in their common time series. FireCCILT11 estimated more BA in each year compared to MCD64A1, and compared to FireCCI51 detected more BA in most years, except 2004, 2005, 2007 and

2008. The year with the largest difference between FireCCILT11 and FireCCI51 was 2001, and FireCCILT11-MCD64A1 was 2013. The FireCCILT11 values were closer to FireCCI51 than MCD64A1, although the FireCCILT11 trend was softer than FireCCI51 and MCD64A1.

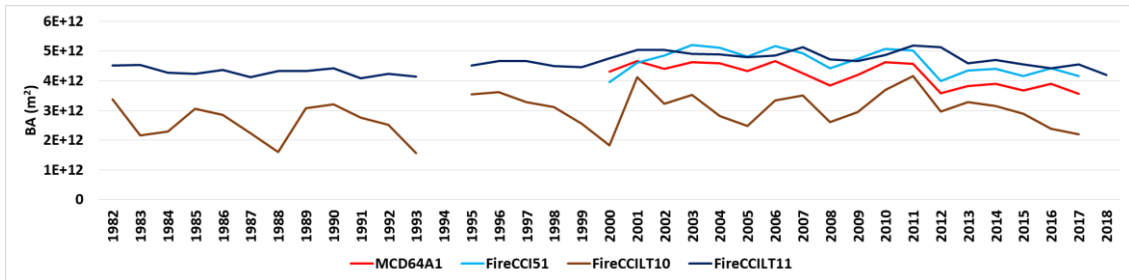


Figure 12. Annual BA (Mkm²) trends of MCD64A1, FireCCI51, FireCCILT10 Beta and FireCCILT11.

Table 4. Annual and month correlation (r Pearson) between BA products. Month correlation between AVHRR2 era months and AVHRR3 era months.

	FireCCI51 Vs FireCCILT11	MCD64A1 Vs FireCCILT11
Annually	0,60	0,87
Monthly	0,95	0,89
	FireCCILT11 1982-2000 Vs FireCCILT11 2001-2018	
Monthly	0,98	

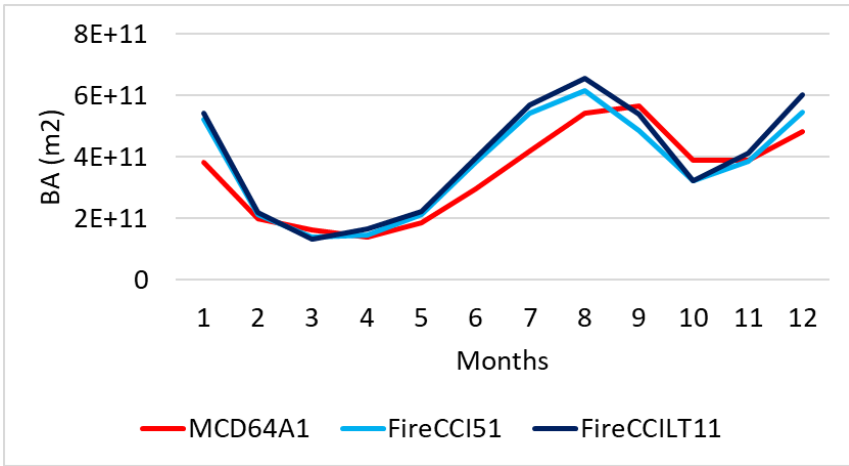


Figure 13. Monthly median trends of the products: FireCCILT11, FireCCI51 and MCD64A1, in the common time series.

The performance of FireCCILT10 Beta is lower than the other products. The new FireCCILT11 has more stable trends and higher accuracy than the Beta product, particularly during AVHRR2 period (1982-2000), when FireCCILT11 was very less affected by the satellites' orbital drift and the number of available observations (Table 5), and presents realistic trends in the same way as for the following years. FireCCILT10 Beta shows significant peaks and unrealistic patterns. The impact of both the number of observations and the solar angle was clearly reduced with the new version of the BA algorithm, particularly for tropical areas. In fact, the median of monthly BA between AVHRR2- AVHRR3 period offers a very high correlation, 0.98, maintaining the monthly trends in the time series.

The analysis of the number of observations, SZA, FireCCILT10 Beta and FireCCILT11 is shown in Table 5. The study analyses the global, tropical and extratropical relation of these variables in the time series of each product where FireCCILT11 offers one more year. The effect of the number of observations and SZA, which hold a negative relation, is lower in FireCCILT11 than in FireCCIL10. The number of observations is highly correlated and explains much of the variability of the SZA, and presents higher values in extratropical regions than tropical regions in both products. The number of observations is less correlated than SZA regarding the BA products although the number of observations also has a relation with the results. The lack of observations has a greater effect in tropical regions, losing BA, and its effect has been diminished in the AVHRR2 period of FireCCILT11. SZA has a negative relation relative to BA products. SZA and FireCCILT10 Beta are highly related in tropical regions and specially explains much of the variability in the AVHRR2 period. FireCCILT11 has solved that relation, the variability explained is low in the AVHRR2 period. The relation is higher in AVHRR3 period but does not affect the BA detected according to Table 4 where the correlation with BA MODIS product is very high.

Table 5. Correlation analysis (r Pearson) between the number of observations, solar angle, and the BA of FireCCILT10 Beta and FireCCILT11 according to Global, tropical and extratropical regions, and the time series of each product. Time periods are grouped as the complete time series, the AVHRR2 period, and the AVHRR3 period.

	#Observations vs. Solar Angle			#Observations vs. BA			Solar Angle vs. BA		
	1982-2017	1982-2000	2001-2017	1982-2017	1982-2000	2001-2017	1982-2017	1982-2000	2001-2017
FireCCILT10 beta									
Global	-0.90	-0.87	-0.87	0.62	0.64	0.41	-0.81	-0.89	-0.62
Tropical	-0.77	-0.59	-0.78	0.47	0.35	0.32	-0.81	-0.89	-0.61
Extratropical	-0.92	-0.91	-0.87	0.29	0.01	0.28	-0.24	0.06	-0.38
FireCCILT11									
Global	-0.82	-0.72	-0.86	0.56	0.12	0.58	-0.62	-0.23	-0.68
Tropical	-0.79	-0.65	-0.83	0.53	0.17	0.37	-0.63	-0.36	-0.62
Extratropical	-0.81	-0.71	-0.85	-0.07	-0.02	0.61	0.14	0.33	-0.54

2.2 Regional comparison with MODIS BA products

The comparison of the average BA products (2001-2018) in continental regions is shown in Table 4. Similar values were found among the MODIS products and FireCCILT11. FireCCILT11 is more burned in the most continental regions of the world. African regions offer the highest BA values in the three products, being FireCCILT11 higher than the MODIS products. FireCCILT11 and FireCCI51 detected in general a similar BA quantity, while MCD64A1 had in most cases lower values. In Australia, FireCCILT11 detects BA between the MODIS products although closer to high values of MCD64A1. Boreal regions offer equal values in BONA in the BA products and similar values in BOAS between FireCCI products but lower in MCD64A1. The lowest burned region changes among products: EQAS in FireCCILT11, MIDE in FireCCI51 and EURO in MCD64A1.



Table 6. Average BA in the continental regions for the MODIS (FireCCI51, MCD64A1) and AVHRR-LTDR (FireCCILT11) products in the common time series (2001-2018). Boreal North America (BONA), Temperate North America (TENA), Central America (CEAM), Northern Hemisphere South America (NHSA), Southern Hemisphere South America (SHSA), Europe (EURO), Middle East (MIDE), Northern Hemisphere Africa (NHAF), Southern Hemisphere Africa (SHAF), Boreal Asia (BOAS), Central Asia (CEAS), Southeast Asia (SEAS), Equatorial Asia (EQAS) and Australia and New Zealand (AUST).

		Continental regions								
		BONA	TENA	CEAM	NHSA	SHSA	EURO	MIDE		
BA (Mkm ²)	FireCCI51	0,45	0,57	0,41	0,98	4,60	0,33	0,25		
	MCD64A1	0,45	0,51	0,49	0,96	5,16	0,19	0,25		
	FireCCILT11	0,45	0,79	0,51	1,05	5,48	0,46	0,47		
			NHAF	SHAF	BOAS	CEAS	SEAS	EQAS	AUST	
	FireCCI51	27,19	29,77	2,94	4,23	2,60	0,26	8,67		
	MCD64A1	23,00	27,24	1,68	3,51	2,49	0,27	9,23		
	FireCCILT11	27,37	29,85	2,77	4,66	2,79	0,32	9,20		

Figure 14 shows the temporal variation of BA in the different continental regions for the three BA products. Trends were similar in most of the regions in the common time series. BONA, NHSA, NHAF, SHAF presented analogous trend and values in the BA products. CEAM, BOAS, EQAS and AUST had similar trends and values with slight differences in isolated years or abrupt peaks where FireCCILT11 had softer trends than the MODIS products. In TENA, SHSA, CEAS and SEAS, FireCCILT11 detected similar values of the MODIS products but FireCCILT11 trends were smoother although they conserved the main peaks and trends. Only in regions with little burned area (EURO or MIDE), the estimations were different, although the trends were similar.

Furthermore, the correlation between SZA and FireCCILT11 (Table 7) is lower or does not exist according to continental regions. Especially, the AVHRR2 period offers the lowest relations where there were the biggest effects. Tropical regions, more affected by SZA, have low correlations and SZA does not explain the variability in FireCCILT11. The AVHRR3 period has some higher relations but they are low and do not affect to the BA detected (Figure 14).

Table 7. Correlation analysis (r Pearson) between the SZA and FireCCILT11 according to Continental regions.

	BONA	TENA	CEAM	NHSA	SHSA	EURO	MIDE
1982-2000	-0,22	-0,36	-0,30	-0,26	0,19	-0,22	-0,48
2001-2018	-0,42	-0,60	-0,26	-0,03	0,11	-0,32	-0,56
	NHAF	SHAF	BOAS	CEAS	SEAS	EQAS	AUST
1982-2000	0,21	0,32	-0,06	-0,34	-0,09	0,31	0,23
2001-2018	0,38	0,31	-0,34	-0,57	0,10	0,07	0,02

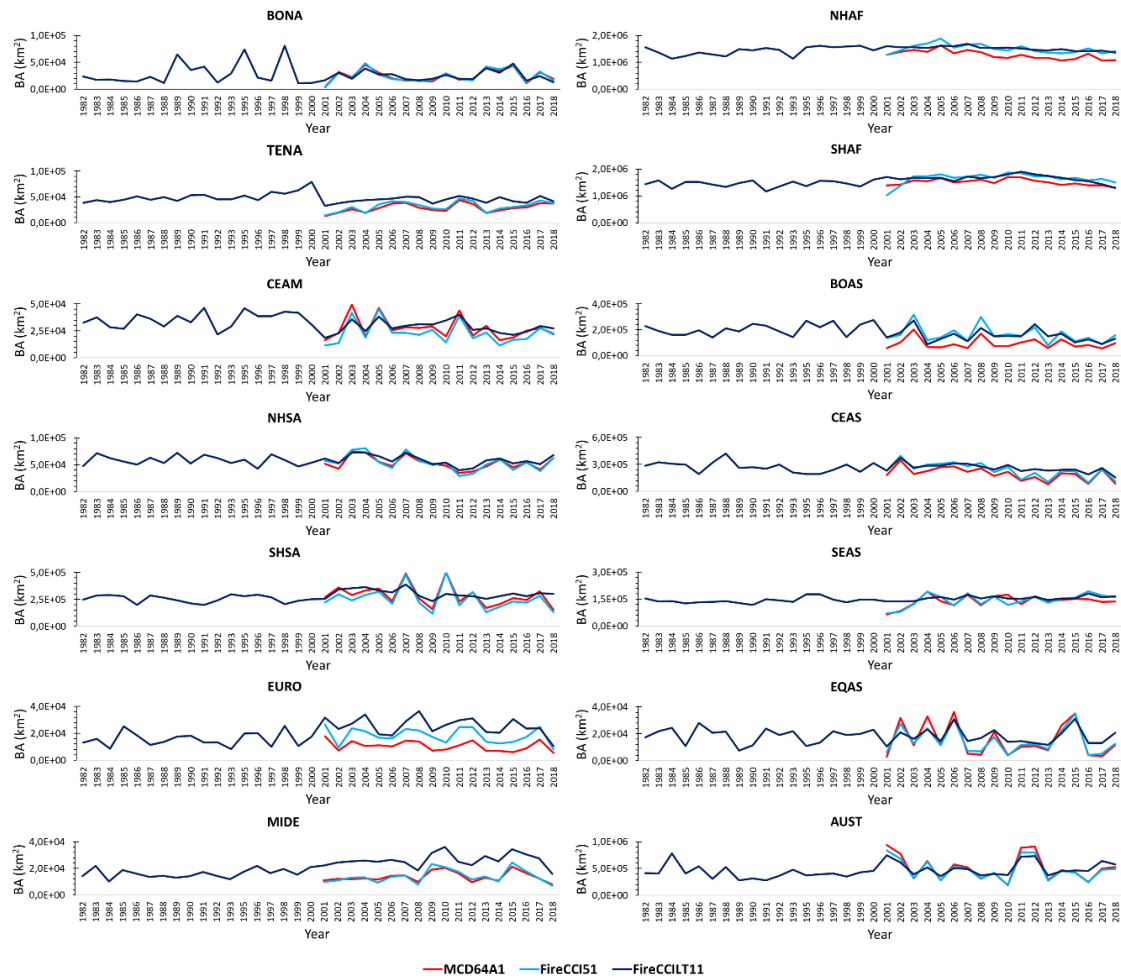


Figure 14. Annual BA trends of MCD64A1, FireCCI51 and FireCCILT11 in the different continental regions (year 1994 excluded).

2.3 Comparison with reference fire perimeters and regional BA products

Official perimeters are compared among the BA products (MCD64A1, FireCCI51, FireCCILT10 Beta and FireCCI51) in Figure 15 and a correlation analysis of FireCCILT11 is made with these official perimeters (Table 8). Australia has the official perimeters with most fire occurrence. The official trends are very similar among all BA products except FireCCILT10 Beta. FireCCI BA products have more underestimation than MCD64A1 in Australia. Even so, FireCCILT11 presents a very high correlation of 0.89 in the common time series (2000-2018).

Canadian official perimeters offer a very similar trend in all BA products except FireCCILT10 Beta, and the AVHRR2 period is analogous between official perimeters and FireCCILT11. The correlation is high and similar in the AVHRR2 (0.85) and the AVHRR3 (0.84) periods. The incorporation of a Boreal model proved to be particularly efficient in this area, which was clearly underestimated by the beta version (FireCCILT10). Official Alaskan perimeters have a similar trend in all BA products except FireCCILT10 Beta, which is deficient in boreal regions. The trends in the AVHRR2 period are analogous. Some underestimation of FireCCILT11 is found in BA peaks of the official perimeters but the correlation is very high, 0.99 in the 2001-2018 period and 0.91 in the 1982-2000 period. MTBS in this case, shows very high accuracy in the 2001-2017 period (r Pearson of 1.00) but 1984-2000 period has a lower

performance of 0.79. Therefore, FireCCILT11 has a high result in AVHRR2 period than MTBS.

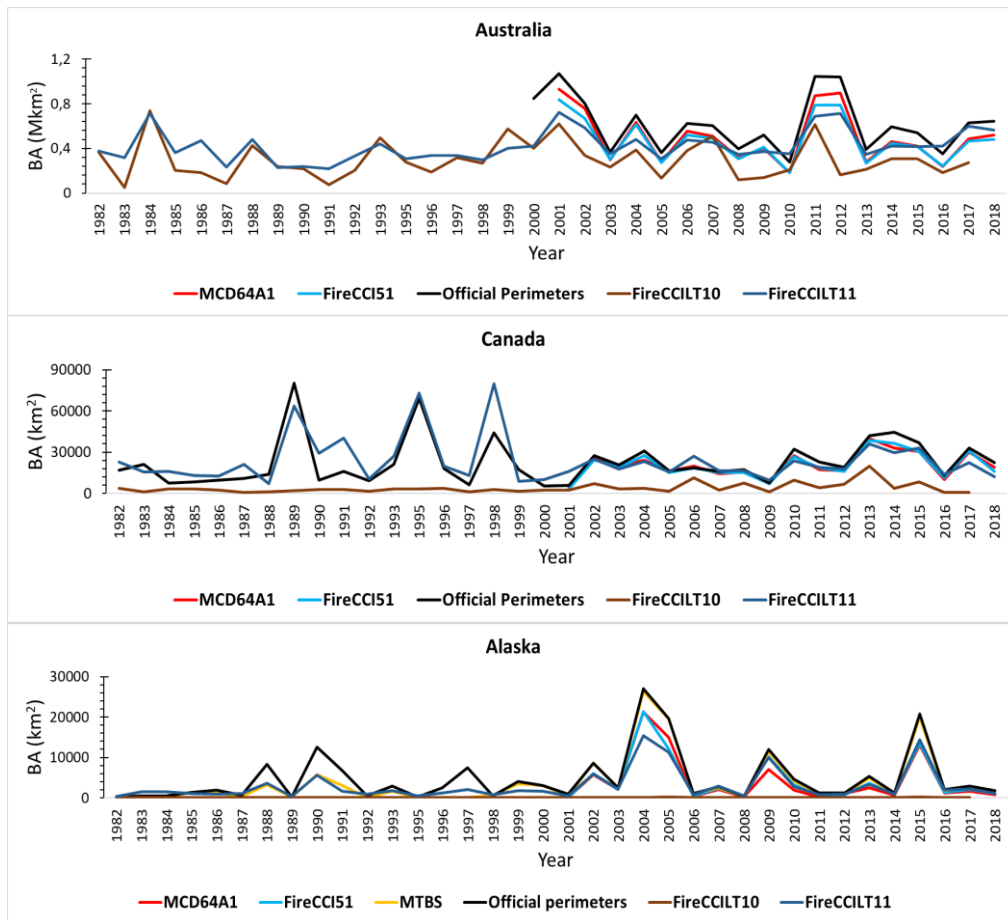


Figure 15. Comparison of BA trends among national official perimeters and BA products (year 1994 excluded).

Table 8. Correlation analysis (r Pearson) between FireCCILT11 in different regions, and the official perimeters and regional BA products. Time periods are grouped as the complete time series with official perimeters, the AVHRR2 period, and the AVHRR3 period.

Official perimeters Vs FireCCILT11				Official perimeters Vs MTBS	
Australia		Canada		Alaska	
2000-2018	0,89	1982-2018	0,81	1982-2018	0,96
2000-2001	-	1982-2000	0,85	1982-2000	0,91
2001-2018	0,94	2001-2018	0,84	2001-2018	0,99
USA					
MTBS Vs FireCCILT11		FireCCI51 Vs FireCCILT11		FireCCI51 Vs MTBS	
1984-2017	0,06	-	-	-	-
1984-2000	0,41	-	-	-	-
2001-2017	0,61	2001-2018	0,71	2001-2017	0,89

USA (continental without Alaska) is inter-compared only among BA products. Figure 16 shows the BA trends where FireCCI51 and MCD64A1 are very similar; MTBS has a bit less detection but high correlation (0.89) with FireCCI51, and FireCCILT11 has more BA detected but less relation (0.71) with FireCCI51 but is still high (Table 8). MTBS has slightly more accuracy in the AVHRR3 period than FireCCILT11. MTBS and FireCCILT10 have a more similar performance in the AVHRR2 period than FireCCILT11, but there are no official perimeters to show the accuracy, only a higher value of FireCCILT11 in Alaska than MTBS in the 1982-2000 period.

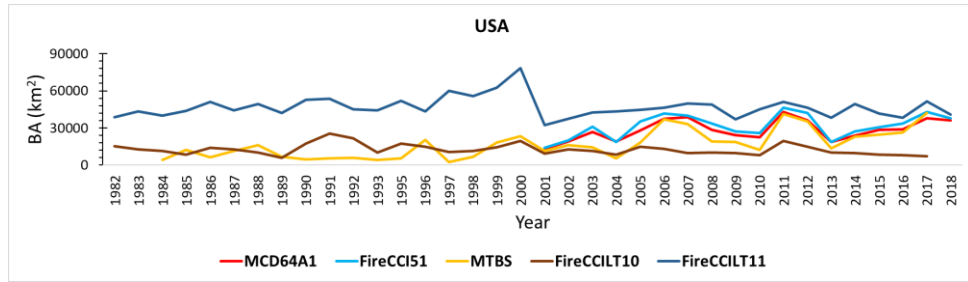


Figure 16. Comparison of BA trends among BA products in the US (year 1994 excluded).

2.4 Comparison with regional BA studies

We further compared the product with existing regional studies (Figure 17 and Table 9), although in this case the uncertainty was higher, as those products included also potential errors. In the case of the Russian republic of Kalmykia study (Dubinin et al. 2010), BA products shows a similar trend with lower BA estimation than FireCCILT11. BA of Dubinin et al. (2010) has an analogous pattern of MODIS products and a related trend with FireCCILT11. Dubinin et al. (2010) detect less BA than FireCCILT11 but these studies have a high correlation in the AVHRR2 period of 0.84 and in the AVHRR3 period of 0.89. In the Siberia study (García-Lázaro et al. 2018), the patterns are very similar in the MODIS era. García-Lázaro et al. (2018) and FireCCILT11 have a correlation of 0.96, but the performance of each is very different in the pre-MODIS era where r Pearson is of 0.17. The García-Lázaro et al. (2018) study assume a fully burned pixel (0.05°) if it is detected, and FireCCILT11 does not, it assigns proportions. Therefore, García-Lázaro et al. (2018) shows a higher BA detection in the period 1982-2000 but it has $\approx 70\%$ less burned pixels than FireCCILT11.

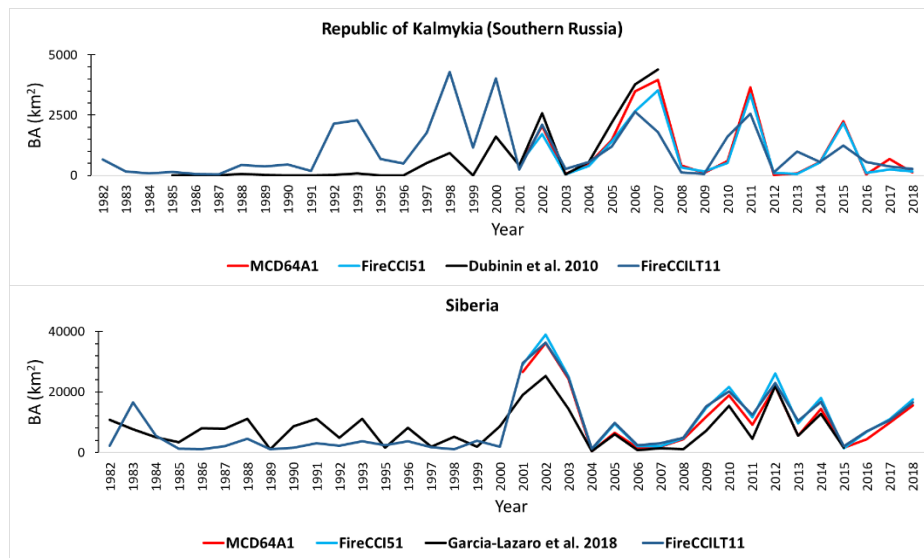


Figure 17. Comparison between BA products using regional studies (year 1994 excluded).

Table 9. Correlation analysis (r Pearson) between FireCCILT11 and the regional BA studies. Time periods are grouped as the complete time series with regional BA studies, the AVHRR2 period, and the AVHRR3 period.

Republic of Kalmykia (Southern Russia)		Siberia	
1985-2007	0,48	1982-2015	0,79
1985-2000	0,84	1982-2000	0,17
2001-2007	0,89	2001-2015	0,96

	Fire_cci ATBD AVHRR-LTDR	Ref.:	Fire_cci_D2.1.3_ATBD-AVHRR-LTDR_v1.0		
		Issue	1.0	Date	19/11/2021
		Page	47		

Annex 3: Validation

1 Validation basis

1.1 Landsat dataset

The validation of low resolution with high resolution is a controversial topic, since if the spatial resolution pixel size of high resolution is used to validate, it would generate unrealistic measures (Boschetti et al. 2006). Therefore, the option of high resolution resampled to spatial resolution pixel size of low resolution, is used to validate low-resolution product. Low resolution has less data variance and reduced information, resampling high resolution decreases the variance (Justice et al. 1989) and allows a fair comparison. Independent reference data has to be developed to accurately assess a product (Justice et al. 2000). Thereby, a Landsat dataset is created satisfying the SAFNet boundaries (Roy et al. 2005) where BA is mapped in the common region between the Landsat images used, in the period between the images and masking non-interpretable areas. Additionally, Long units (consecutive pairs of images) of Landsat are generated because these are more adequate in low resolution products without active fires to reduce the influences of temporal accuracy (Lizundia-Loiola et al. 2020; Padilla et al. 2018). Long unit dataset is developed in Africa in a place with the largest availability of images on the continent (Southeast of Angola) according to Wulder et al. (2016) from 1989 to 2018, and 183 images are used in total. Africa is selected because it is the most burned region (Lizundia-Loiola et al. 2020) and we seek a scene which is cloud-free as long as possible. The objective was to map the fire season, and all the consecutive available images are included, although it is not possible to achieve the same temporal coverage in all years. Some years only have 3 consecutive images available (1992, 1997, 2007 and 2008), others only 2 (2009 and 2012) and others, only one or none (before 1989, 1999, 2000 and 2010). In addition, some years have non-interpretable areas (1998 and 2006) or Landsat 7 SLC-off gaps (2003, 2004, 2007, 2009, 2011 and 2012). Therefore, obtaining a long-term data set of independent reference data has many limitations and problems. The location to be studied is described by large fires (Ramo et al. 2021) in the central months of the fire season but with a light burned signal. The first months of the fire season are characterized by small fires (Lizundia-Loiola et al. 2020). Despite not satisfying the CEOS-LPVS protocols, we use more images (183) and years (27) than other studies such as Roy et al. (2005) where in 11 African locations use 53 images in a single year (2001), Boschetti et al. (2006) use 33 Landsat scenes and images in 2000, and Roy and Boschetti (2009) use 11 Landsat (consecutive acquisitions) in 2001. MCD64A1 validation uses a similar number of images in 108 Landsat scenes (consecutive acquisitions).

1.2 Pareto Boundary

Previous statistics (Section 0) can be misleading in low resolution if we do not have a reference. It may be that a high commission and omission error mean poor accuracy of a product but if a ground truth categorized or a high resolution also offer high values error, the low resolution product is demonstrating a good performance. We cannot ask for more accuracy in a low-resolution product than a high-resolution dataset. Therefore, we need a methodology that shows what we can expect from low-resolution and what not. Pareto boundary methodology (Boschetti et al. 2004) accomplish that function which is derived from the previous statistics. This method says if the accuracy of the product studied is due to either the performance of the algorithm or the low resolution. Initially, Pareto boundary is generated to binary classifications but it can be adapted to

proportions. In addition, that method is developed to work with the same resolutions, which means that high resolution should be resampled to the low resolution. High resolution resampled (Hr), which maintains BA proportions, is categorized in different BA percentages (0%, 10%, 20%, n%) and binarised (Hb, burned-unburned), dichotomy classifications (Hb) are obtained and are validated against High resolution resampled (Hr). Boundary curve is the trade-off between omission and commission error developed between high-resolution resampled (Hr) and the dichotomy classifications (Hb). A binary low-resolution (Lbr) product could never pass the boundary curve because its spatial resolution does not hold so much accuracy. But a low resolution proportion (Lr) product can in fact do it, if a performance is very accurate (Boschetti et al. 2004). We have done two analyses with Pareto boundary: First, low resolution (Lr) product is categorized (Lbr) according to proportions (0% 10%, 20%, n%) and validated with High resolution resampled (Hr) to learn whether our product follows a similar trend according to BA proportions. Secondly, low-resolution (Lr) product is validated with High resolution resampled (Hr) to identify the true accuracy of our product with reference data. In both cases, omission and commission error are calculated.

Pareto Boundary has been used in several studies of low resolution such as snow studies (Pepe et al. 2010) or BA (Anaya and Chuvieco 2012; Katagis et al. 2014; Moreno-Ruiz et al. 2020; Moreno-Ruiz et al. 2019; Oliva et al. 2011).

2 Results

Landsat dataset is used to validate as an independent reference database. That dataset is different according to the year and presents several limitations. Some years have a reduced number of images that do not allow creation of a consistent long-unit such as the years: 1992, 1995, 1997, 2004, 2007, 2008, 2009 and 2012. Other years have non-interpretable areas, which reduce the study area such as 1998 or 2006. Still, other years (2003, 2004, 2007, 2009, 2012) have a problem in the quality of the data because Scan Line Corrector (SLC) failed in the Landsat 7. Despite all of this, the Landsat dataset is a consistent ground truth and has many years without problems, which means that it is a long-term validation dataset.

Validation between Landsat dataset degraded at low resolution (0.05°) and FireCCILT11 is shown in Table 10. Commission errors are usually lower than omission errors in the time series; although both present low values, there are unbalanced years. The AVHRR2 period has fewer years to validate with that Landsat dataset and has the most unbalanced years. Relative Bias notices underestimation of BA except in some years with limitations, both in the AVHRR2 period and in the AVHRR3 period. The AVHRR2 period has more underestimation. The AVHRR3 period shows higher DC values than the AVHRR2 period although both have years with high DC values. Year 1989 is the best year of the validation years in the AVHRR2 period with a high DC of 0.63. 2014 is the best year of the time series with balanced errors around 10 and DC of 0.87.

The correlation in the time series between Landsat dataset and FireCCILT11 is 0.53, in the AVHRR2 period is 0.52 and in the AVHRR3 period is 0.72.

Table 10. Validation outcomes between the FireCCILT11 and the long-term degraded Landsat dataset. Purple represents the years when the Landsat period is lower or equal to one and a half months, and the long-unit is minimal (2-4 scenes Landsat); Blue is used when there are non-interpretable areas and the study area is reduced; Yellow, when there are Landsat 7 with SLC-Off, and Brown when the Landsat period is lower or equal to one and a half months and there are Landsat 7 with SLC-Off.

	1989	1990	1991	1992	1993	1995	1996	1997	1998
Commission error	0,23	0,09	0,04	0,00	0,47	0,45	0,11	0,26	0,00
Omission error	0,47	0,57	0,74	1,00	0,40	0,96	0,90	0,95	0,90
real Bias	-0,31	-0,53	-0,73	-1,00	0,13	-0,93	-0,89	-0,93	-0,90
Dice Coefficient	0,63	0,58	0,41	0,00	0,56	0,07	0,17	0,10	0,17
	2001	2002	2003	2004	2005	2006	2007	2008	2009
Commission error	0,09	0,10	0,42	0,60	0,31	0,14	0,77	0,30	0,40
Omission error	0,41	0,41	0,25	0,37	0,48	0,29	0,21	0,33	0,25
real Bias	-0,35	-0,34	0,30	0,57	-0,24	-0,17	2,46	-0,03	0,26
Dice Coefficient	0,72	0,71	0,66	0,49	0,60	0,78	0,36	0,69	0,67
	2011	2012	2013	2014	2015	2016	2017	2018	
Commission error	0,92	0,47	0,08	0,12	0,07	0,09	0,08	0,21	
Omission error	0,05	0,32	0,24	0,14	0,29	0,34	0,27	0,40	
real Bias	11,25	0,27	-0,17	-0,02	-0,23	-0,28	-0,20	-0,24	
Dice Coefficient	0,14	0,60	0,84	0,87	0,81	0,76	0,81	0,68	

Pareto boundary analysis is shown in Figure 18 for all available years, except 1994. Hypothetical binary FireCCILT11 presents a related curve regarding to boundary curve, which indicates a consistent pattern according to the different percentiles of proportions. The detection of different proportion of burned follows the same pattern in FireCCILT11 as Landsat. FireCCILT11 presents errors close to the boundary curve for most years, improving highly a hypothetic binary FireCCILT11. FireCCILT11 never even has a higher error than binary FireCCILT11, showing an adequate performance of the proportions. Despite some years in Table 10 with high errors, Pareto boundary shows a high performance of the algorithm and the main cause of high errors is due to spatial resolution. A great example is 1996 where there is a high Omission error and low DC, but FireCCILT11 is beneath boundary curve, which shows a good performance of the algorithm. Improvement is possible for some years, bringing them closer to boundary curve but the performance of FireCCILT11 is high and some years are in the boundary curve or beneath of it. The AVHRR2 period presents results similar to the AVHRR3 period, and shows a high performance of the algorithm that only in Table 10 is not possible to display. The behaviour of FireCCILT11 is higher than a dichotomy product, even if that is high resolution degraded. The validation of FireCCILT11 (Table 10) and Pareto boundary methodology (Figure 18) show a consistent and coherent product in the whole time series.



fire
cci

Fire_cci
ATBD AVHRR-LTDR

Ref.: Fire_cci_D2.1.3_ATBD-AVHRR-LTDR_v1.0

Issue 1.0

Date 19/11/2021

Page

50

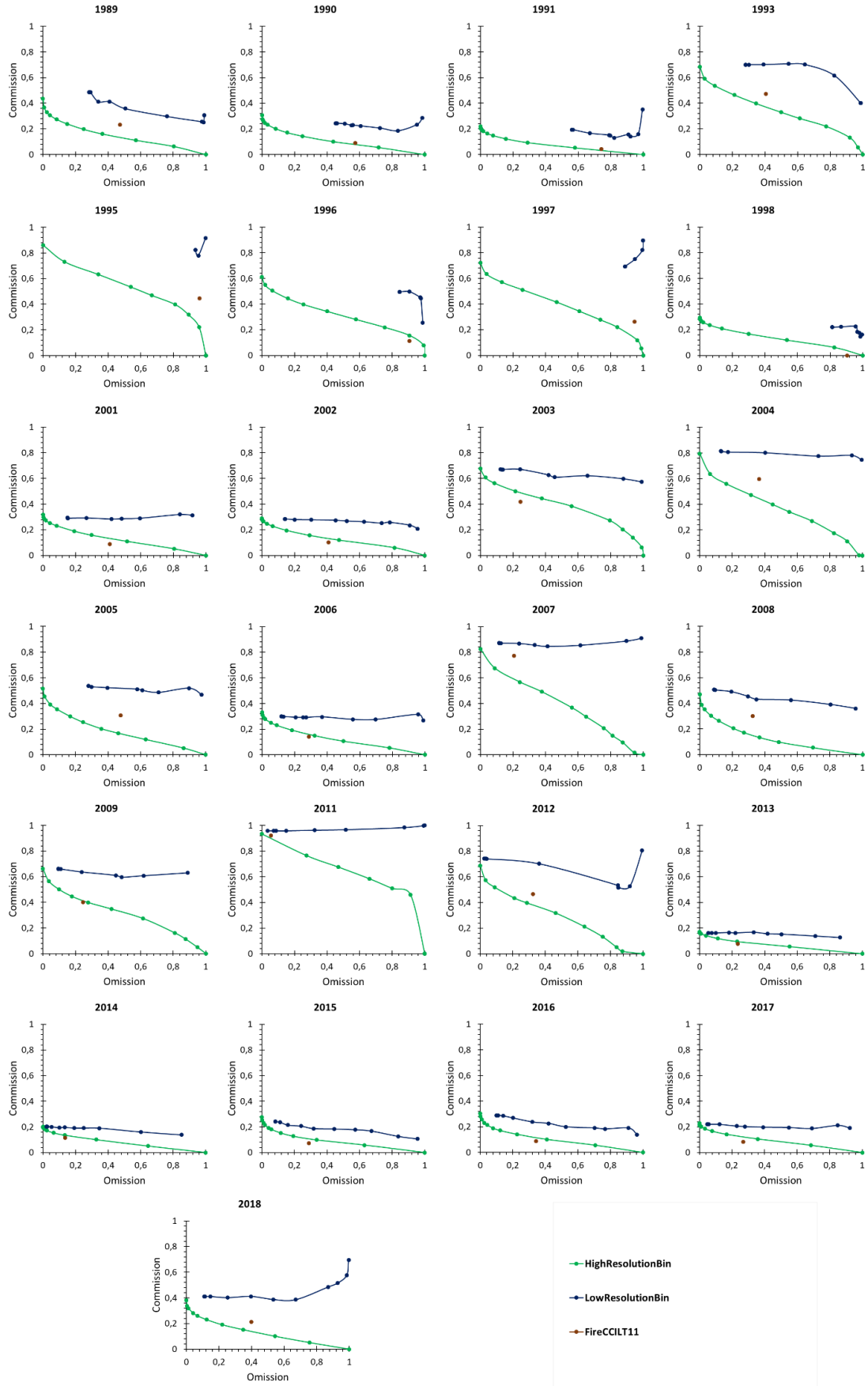


Figure 18. Pareto boundary with a long-term Landsat dataset, which is resampled at low resolution and binarised in percentiles of proportions (green), FireCCILT11 binarised according with percentiles of proportion (blue) and FireCCILT11 (brown).